

A Spectral Rotary Analysis of Gravity Waves: An Application during one of the SOUTHTRAC Flights

Alejandro de la Torre¹, Peter Alexander², Tomás Marcos¹, Rodrigo Hierro¹, Pablo Llamedo¹, Jose Luis Hormaechea³, Peter Preusse⁴, Markus Geldenhuys⁵, L. Krasauskas⁵, Andreas Giez⁶, Bernd Kaifler⁷, Natalie Kaifler⁷, and Markus Rapp⁸

¹Universidad Austral

²IFIBA

³Facultad de Ciencias Astronomicas y Geofisicas UNLP

⁴Juelich Research Center

⁵Institute of Energy and Climate Research (IEK-7: Stratosphere), Forschungszentrum Jülich

⁶Deutsches Zentrum für Luft- und Raumfahrt

⁷Institute of Atmospheric Physics, German Aerospace Center

⁸Deutsches Zentrum für Luft- und Raumfahrt (DLR)

November 22, 2022

Abstract

To understand the main orographic and non-orographic sources of gravity waves (GWs) over South America during an Experiment (Rapp et al, 2021, <https://doi.org/10.1175/BAMS-D-20-0034.1>), we propose the application of a rotational spectral analysis based on methods originally developed for oceanographic studies. This approach is deployed in a complex scenario of large-amplitude GWs by applying it to reanalysis data. We divide the atmospheric region of interest into two height intervals. The simulations are compared with lidar measurements during one of the flights. From the degree of polarization and the total energy of the GWs, the contribution of the upward and downward wave packets is described as a function of their vertical wavenumbers. At low levels, a larger downward energy flux is observed in a few significant harmonics, suggesting inertial GWs radiated at polar night jet levels, and below, near to a cold front. In contrast, the upward GW energy flux, per unit area, is larger than the downward flux, as expected over mountainous areas. The main sub-regions of upward GW energy flux are located above Patagonia, the Antarctic Peninsula and only some oceanic sectors. Above the sea, there are alternating sub-regions dominated by linearly polarized GWs and sectors of downward GWs. At the upper levels, the total available GW energy per unit mass is higher than at the lower levels. Regions with different degrees of polarization are distributed in elongated bands. A satisfactory comparison is made with an analysis based on the phase difference between temperature and vertical wind disturbances.

1 **A Spectral Rotary Analysis of Gravity Waves: An Application during one of**
2 **the SOUTHTRAC Flights**

3 A. de la Torre¹, P. Alexander², T. Marcos¹, R. Hierro¹, P. Llamedo¹, J.L. Hormaechea³, P.
4 Preusse⁴, M. Geldenhuys^{4,5}, L. Krasauskas⁴, A. Giez⁶, B. Kaifler⁷, N. Kaifler⁷ and M. Rapp^{7,8}

5 ¹LIDTUA(CIC) and CONICET, Facultad de Ingeniería, Universidad Austral, Pilar, Argentina.

6 ²Instituto de Física de Buenos Aires, CONICET, Buenos Aires, Argentina.

7 ³ Estación Astronómica Río Grande, Facultad de Ciencias Astronómicas y Geofísicas, Universidad Nacional de La
8 Plata, and CONICET, La Plata, Argentina.

9 ⁴Institute of Energy and Climate Research (IEK-7), ForschungszentrumJülich, Jülich, Germany.

10 ⁵South African Weather Service, Private Bag X097, Pretoria 0001, South Africa.

11 ⁶Einrichtung Flugexperimente, Deutsches Zentrum für Luft- und Raumfahrt, Oberpfaffenhofen, Germany.

12 ⁷Institut für Physik der Atmosphäre, Deutsches Zentrum für Luft- und Raumfahrt, Oberpfaffenhofen, Germany.

13 ⁸Meteorologisches Institut München, Ludwig-Maximilians-Universität München, Munich, Germany.

14 Correspondingauthor: Alejandro de la Torre (adelatorre@austral.edu.ar)

15 **Key Points:**

- 16 • A rotary spectral analysis is proposed to classify possible sources of gravity waves
17 according to their degree of polarization.
- 18 • From reanalysis data, the method is applied at a selected position during one of the flights
19 of the SOUTHTRAC-GWExperiment.
- 20 • Upward and downward gravity wave structures from orographic and non-orographic
21 origin with different degrees of polarization are observed.

22 **Abstract**

23 To understand the main orographic and non-orographic sources of gravity waves (GWs) over
24 South America during an Experiment (Rapp et al, 2021, [https://doi.org/10.1175/BAMS-D-20-](https://doi.org/10.1175/BAMS-D-20-0034.1)
25 0034.1), we propose the application of a rotational spectral analysis based on methods originally
26 developed for oceanographic studies. This approach is deployed in a complex scenario of large-
27 amplitude GWs by applying it to reanalysis data. We divide the atmospheric region of interest
28 into two height intervals. The simulations are compared with lidar measurements during one of
29 the flights. From the degree of polarization and the total energy of the GWs, the contribution of
30 the upward and downward wave packets is described as a function of their vertical
31 wavenumbers. At low levels, a larger downward energy flux is observed in a few significant
32 harmonics, suggesting inertial GWs radiated at polar night jet levels, and below, near to a cold
33 front. In contrast, the upward GW energy flux, per unit area, is larger than the downward flux, as
34 expected over mountainous areas. The main sub-regions of upward GW energy flux are located
35 above Patagonia, the Antarctic Peninsula and only some oceanic sectors. Above the sea, there are
36 alternating sub-regions dominated by linearly polarized GWs and sectors of downward GWs. At
37 the upper levels, the total available GW energy per unit mass is higher than at the lower levels.
38 Regions with different degrees of polarization are distributed in elongated bands. A satisfactory
39 comparison is made with an analysis based on the phase difference between temperature and
40 vertical wind disturbances.

41 **Plain Language Summary**

42 Atmospheric gravity waves (GWs) are of great importance in the transport of energy and
43 momentum through the atmosphere. Their sources can be broadly classified as stationary and
44 non-stationary. The southern tip of South America represents one of the most important natural
45 laboratories for detecting the coexistence of large-amplitude GWs. We present a spectral method
46 to establish a semi-quantitative classification of the different groups of GWs and their main
47 vertical direction of propagation. We apply the method on the basis of global model data. We
48 divide the lower and middle atmosphere into two vertical intervals and compare the model with
49 data from one of the instruments deployed during the experiment. From the degree of
50 polarization of the GWs, we describe the net contribution of the upward and downward wave
51 packets as a function of their spectral harmonics. The main subregions of upward gravity wave

52 energy flux alternate with subregions dominated by linearly polarized GWs and downward
53 gravity wave sectors mainly above the ocean. At the upper levels, the total available GW energy
54 per unit mass is higher than at the lower levels. A comparison is made between these results and
55 an independent analysis based on the known polarization relations for GWs.

56 **1 Introduction**

57 The complex structure inherent to frequently observed atmospheric gravity wave (GW)
58 ensembles constitutes a challenge that remains difficult to address (e.g., P. Alexander et al.,
59 2015a, b; de la Torre et al., 2019; Fritts & M.J. Alexander, 2003; Wickert et al., 2020). This is
60 mainly due to the time and space constraints imposed by the observational windows and by the
61 complexity of the atmospheric wave structures and other present phenomena (M.J. Alexander,
62 1998; Wu et al., 2006). The following basic classification of the main GW sources are: the flow
63 of the air forced by the orography (called mountain waves (MWs)), atmospheric convection, and
64 the spontaneous emission after geostrophic adjustment of the flow in the vicinity of jets and
65 fronts (Fritts & M.J. Alexander, 2003; Plougonven & Zhang, 2014; Zhang et al., 2004). In
66 particular, the usual assumption describes a scenario with dominant monochromatic linear GWs,
67 which would explain the transport of large fractions of the wave energy and momentum flux
68 through different atmospheric levels and synoptic conditions.

69 In a relatively simple GW scenario, the hodographic technique (see e.g., Gubenko et al., 2020;
70 Vincent, 1984) requires a single coherent wave leading to the fluctuations that perturb the
71 horizontal velocity profile. For a single, linear, steady, non-dissipating, elliptically polarized
72 wave in a region with negligible vertical shear in the background wind (Eckermann, 1996), the
73 intrinsic frequency of the GWs can be obtained by the axial ratio of the ellipse (Cot & Barat,
74 1986), its horizontal propagation axis by the orientation of the ellipse major axis (Vincent
75 & Fritts, 1987) and the direction of the GWs vertical group velocity by the sense of ellipse
76 rotation with height (Hirota & Niki, 1985). However, Eckermann & Hocking (1989) demonstrated
77 that hodographic analyses of profiles that contained a large number of GWs sometimes yielded
78 results that reflected the statistical properties of random incoherent fluctuations, rather than the
79 polarization characteristics. Nevertheless, the isolation and characterization of GWs when the
80 wave field consists mainly of a few monochromatic waves are quite straightforward.

81 From another perspective, spectral techniques allow searching for coherent waves within various
82 traceable wavelength bands. These methods are especially useful when the distribution of GW
83 energy is broadly assigned to wave packets with very different wavelengths, frequencies and
84 amplitudes (e.g., Hines, 1991). This may be a typical scenario in the geographic region
85 considered in this study. The analysis of the polarization characteristics of the GW spectrum may
86 provide a valuable semi-quantitative characterization of the GW ensemble (Eckermann, 1996;
87 Gonella, 1972; Leaman & Sanford, 1975; Mooers, 1973), specifically their dominant intrinsic
88 frequencies or wavelengths, vertical propagation direction of GW and GW energy and
89 momentum fluxes. This approach has been applied in the past to oceanic GWs (e.g., Leaman &
90 Sanford, 1975).

91 A classification of GWs by their sources is proposed: orographic (linearly polarized (LP)) or
92 non-orographic (elliptically polarized (EP)). This classification is based on their degree of
93 polarization. As is well known, the degree of polarization also corresponds to non-hydrostatic,
94 hydrostatic non-rotating or rotating GWs, following their intrinsic frequency regimes (e.g. Gill,
95 1982, Section 8.8). From For the polarization relations for the complex amplitudes of the zonal
96 and meridional perturbation velocity components (Vadas, 2013 –equation (B3); P. Alexander et
97 al., 2022 –equation (1)), it may be seen that an ellipse links both horizontal velocity components,
98 whereby the eccentricity equals the ratio of GW inertial to intrinsic frequency. As the
99 eccentricity lies between 0 and 1, a value close to 1 indicates a wave linearly polarized, which
100 corresponds to an intrinsic frequency close to the buoyancy frequency, within the non-
101 hydrostatic regime. An alternative to this proposal may be to rely on their time dependence
102 (stationary or non-stationary, respectively). In the present analysis, we will illustratively apply
103 the method considering model simulations with high spatial resolution at a fixed time. We leave
104 the time dependence classification based on mesoscale simulations for a future contribution.

105 The geographic region considered in this study includes the southern Andes, Patagonia, the
106 Antarctic Peninsula and the surrounding oceanic areas. It exhibits the world's strongest hotspots
107 of GW activity, taking place mainly during austral winter and early spring (e.g., P. Alexander et
108 al., 2010; de la Torre et al., 2012; Fritts et al., 2016; Hoffmann et al., 2013; Llamedo et al.,
109 2019; Rapp et al., 2021). An intense MW activity was observed by other studies above and to
110 the lee of the mountains, given the prevailing strong tropospheric westerly winds. Strong GW

111 activity is observed in the middle to upper stratosphere along 60°S, from the Drake Passage to
112 the South Pacific (see, e.g., Ern et al., 2006; Hindley et al., 2015; M. J. Alexander et al., 2010].
113 This circumpolar belt of almost zonally symmetric GW activity is related to strong momentum
114 fluxes and is sometimes referred to as the GW belt.

115 A precursory experiment to the one referred in this study, also performed in the southern
116 hemisphere in winter, was the Deep Propagating GW Experiment (DEEPWAVE) (Fritts et al.,
117 2016). It was conducted by several research flights with two aircraft from Christchurch, New
118 Zealand, involving various ground-based instruments, satellite datasets, and a variety of
119 numerical models (Bramberger et al., 2017; Fritts et al., 2016; Gisinger et al., 2017; Portele et al.,
120 2018; Smith et al., 2016). The Southern Hemisphere Transport, Dynamics, and Chemistry–
121 Gravity Waves (SOUTHTRAC-GW) mission, performed in September 2019, was based on a
122 synchronized multiple experimental platform. During this experiment, the complexity of the
123 interacting ensemble of GW activity below the mesopause, at extratropical southern latitudes
124 was again observed, as expected (Rapp et al. 2021). The experiment consisted in deploying three
125 main instruments dedicated to the measurement of GW signatures. In particular, the Airborne
126 Lidar for Middle Atmosphere research (ALIMA), a compact upward-pointing Rayleigh lidar
127 using a pulsed neodymium-doped yttrium aluminum garnet laser (Kaifler et al., 2020). The
128 campaign objectives are described in Rapp et al (2021). SOUTHTRAC-GW was the first airborne
129 field campaign devoted to GW dynamics in the atmosphere from the troposphere up to the
130 mesopause (5 to 80 km altitude) in the region considered here (Rapp et al., 2021). During the
131 experiment, 7 successful flights spanning a total of 60 hr were completed. The campaign period
132 coincided with the occurrence of a sudden stratospheric warming which created critical level
133 conditions at about 40 km altitude (Dörnbrack et al, 2020). Among many parameters,
134 measurements from temperature (T) and zonal (u), meridional (v) and vertical (w) wind
135 components were obtained. A preliminary analysis of the measurements and model results
136 revealed strong evidence for MW excitation over the Andes and subsequent vertical as well as
137 horizontal propagation, including refraction and downwind advection into the polar night jet and
138 along the GW belt (Rapp et al., 2021).

139 In order to interpret the observations, the sources of GWs and their propagation direction is very
140 important. Our main aim, after describing a rotary spectral method capable of detecting the

141 spatial distribution of dominant up- and down going GW energy, is to apply it to a
142 SOUTHTRAC case study. We selected one of the first flights, identified as ST08, performed
143 from 11 September at 23:05:36 UTC to 12 September 2019 at 07:21:14 UTC (Rapp et al., 2021).
144 The The method is based on the determination of the dominant degree of polarization of the GW
145 ensemble, as a function of the vertical wavenumber, height interval and geographic sector,
146 above the southern Patagonia, Drake Passage and Antarctic Peninsula. Stationary waves are
147 expected to be mostly linearly polarized (LP) and are included in the analysis. The method is
148 illustrated for a fixed time selected after the beginning of one of the HALO flights, when the
149 reanalysis data are available. ST08 was the flight with the best conditions for excitation and deep
150 mountain wave propagation and we chose the time when HALO crossed the highest mountains
151 for our reanalysis. The selected altitude ranges include the tropospheric and stratospheric
152 regions.

153 Section 2 introduces the spectral rotary method. In Section 3, the model and experimental data,
154 the expected limitations derived from the observational windows and the available time and
155 space resolution are described. The synoptic conditions and a validation of the simulated T
156 profile against the lidar data are performed at the fixed selected time. In section 4, the rotary
157 spectra method is applied to reanalysis data at a representative HALO position during one of the
158 SOUTHTRAC-GW flights. We separate the region considered into two non-overlapping tropo-
159 stratospheric and strato-mesospheric altitude intervals. The flight considered in this study reveals
160 an unusually deep propagation of stationary GWs up to mesospheric levels. In section 5, a
161 comparison is made with an independent method consisting in the calculation of the phase
162 differences between T and wperturbations (T' and w') and from there, the associated vertical
163 horizontal momentum flux. Section 6 provides a discussion and some conclusions that should
164 also be taken into account in future analyses and remaining case studies of the SOUTHTRAC-
165 GW Experiment.

166 **2 Spectral rotary analysis (SRA)**

167 As pointed out by Eckermann (1999), three statistical approaches may be used to characterize the
168 polarization ellipses defined from horizontal wind velocity perturbation data: the hodographic
169 method analysis (e.g., Cadet & Teitelbaum, 1979; Cot & Barat 1986; Vincent, 1984; Vincent &
170 M. J. Alexander, 2020), the cross-spectral analysis (e.g., Cho, 1995), and the spectral rotary

171 analysis (e.g., Eckermann & Vincent, 1989). As stated by Eckermann (1999), all three methods
 172 are in some sense equivalent. The appropriate choice will probably depend on the scenario.

173 One particularly general form of the hodographic method is a description in terms of the so-
 174 called Stokes parameters (e.g., Vincent & Fritts, 1987). This is an analysis technique derived
 175 from the electromagnetic waves theory and is well described in many standard textbooks (e.g.,
 176 Mishchenko, 2014). According to this method, any partially polarized wave motion can be
 177 described completely and uniquely in terms of its Stokes parameters. Vincent & Fritts (1987)
 178 applied such parameters in GW studies. The method assumes that any vertical profile of
 179 horizontal wind velocity perturbations contains a partially polarized coherent wave field
 180 embedded in an unpolarized, isotropic, noise-like background velocity field. The latter is
 181 characterized by a variance equal to the sum of the average of u' and v' variances and a phase
 182 accounting for the elliptical nature of the wave. If this phase is 0° or 180° , it implies a linear
 183 polarization, 90° or 270° implies a circular polarization and any value in between implies an
 184 elliptical polarization. The perturbation velocity vector will rotate anticyclonically with time and
 185 space as one moves in a direction opposite to the phase velocity (Gill, 1982; Placke et al., 2013).
 186 In the southern hemisphere, this means that upgoing waves (downward phase progression)
 187 account for a wind vector that rotates anticlockwise with increasing height, while with
 188 downgoing waves, a clockwise rotation is expected (Vincent, 1984). For atmospheric scenarios
 189 with undeniably complex distributions of coexisting wavepackets, a spectral approach should be
 190 undertaken, in order to recognize the statistically meaningful processes lying within.

191 In the process, a rotary-vector analysis method may be developed based on the assembly of a
 192 complex vector consisting of 2 components of the velocity vector along perpendicular axes, in
 193 particular, the zonal and meridional wind components (e.g., Gonella, 1972; Mooers, 1973).
 194 Below, we adapted the mentioned developments to our purpose. After a Fourier transform of the
 195 horizontal zonal and meridional residual wind components u' and v' :

$$196 \quad u'(z) = \frac{\pi}{2} \int_0^{\infty} [B_1(m) \cos(mz) + B_2(m) \sin(mz)] dm \quad (1)$$

197 and

$$198 \quad v'(z) = \frac{\pi}{2} \int_0^{\infty} [B_3(m) \cos(mz) + B_4(m) \sin(mz)] dm \quad (2)$$

199 the spectral method gives the decomposition of the total available wave energy in terms of the
 200 so-called clockwise and anticlockwise spectra, as a function of the vertical wavenumber (m). In
 201 the present analysis, we choose the vertical z coordinate increasing downwards, following a
 202 convention in the above mentioned previous spectral analyses in the ocean. That is, $z = 0$ at the
 203 highest point of each of the two altitude ranges selected below. If one considers the horizontal
 204 velocity vector to be $u + iv$, where u is the east (real) part of the horizontal velocity and v is the
 205 north (imaginary) part, then, at each m , we can represent the above helix simply by:

$$206 \quad u_m + iv_m = u_+ e^{imz} + u_- e^{-imz} \quad (3)$$

207 with complex constants u_+ and u_- .

208 Then, it may be shown that (e.g., Gonella, 1972):

$$209 \quad |u_+| = \frac{1}{2} [(B_4 + B_1)^2 + (B_3 - B_2)^2]^{1/2} \quad (4)$$

210 and

$$211 \quad |u_-| = \frac{1}{2} [(B_4 - B_1)^2 + (B_3 + B_2)^2]^{1/2} \quad (5)$$

212 The anticlockwise and clockwise components of the energy per unit mass spectrum are given by:

$$213 \quad S_+ = \frac{1}{2} (u_+^* u_+) \quad (6)$$

214 and

$$215 \quad S_- = \frac{1}{2} (u_-^* u_-) \quad (7)$$

216 The integration over m under S_+ and S_- shows the relative contribution of each energy
 217 component. It provides the partition of the total energy. However, it must be stressed that this is
 218 an overestimation of the energy associated with the upgoing and downgoing waves. Low-
 219 frequency GWs are not exactly circularly polarized except near the inertial frequency, but

220 elliptically polarized. Since an elliptically polarized wave can always be resolved into clockwise
 221 and anticlockwise circularly polarized components, even a purely upgoing or downgoing wave
 222 will contribute to both the clockwise and the anticlockwise spectra. In this sense, this analysis
 223 must not be considered as strictly quantitative. Nevertheless, useful statistical information
 224 regarding the prevailing up- or down-propagating GW packets may be obtained and, based only
 225 on the nature of their polarization, their probable sources can be identified.

226 For the present analysis, we define the total rotational energy as

$$227 \quad E_T = S_- + S_+ \quad (8)$$

228 In turn, the difference

$$229 \quad C_R = S_- - S_+ \quad (9)$$

230 will be defined here as the 'rotary coefficient'. It is proportional to the average surface of the
 231 ellipse. Its sign indicates the dominant polarization of the ellipse: positive for clockwise,
 232 negative for anticlockwise. Then, a positive/negative C_R value means
 233 clockwise/counterclockwise rotation with increasing z (namely, counterclockwise/clockwise
 234 with increasing altitude).

235 Additionally, sometimes it is convenient to define the 'normalized rotary coefficient', as it is
 236 bounded in the interval $[-1, 1]$:

$$237 \quad NC_R = (S_- - S_+) / (S_- + S_+) \quad (10)$$

238 In effect, its magnitude will be ± 1 for pure rotary motion and zero for unidirectional (linearly
 239 polarized) motion. To set this out, we write $S_+ = p S_-$, with p real and ≥ 0 , $NC_R = (S_- - p S_-) / (S_- +$
 240 $p S_-) = (1 - p) / (1 + p)$.

241 Next, we calculate and plot C_R and NC_R , as they provide complementary information. For
 242 example, for a given vertical wavenumber m and altitude interval, a latitude-longitude sector
 243 with positive/negative C_R will reveal dominant up-/down-propagating GWs. Besides, if C_R is
 244 close to zero, this may indicate two possible structures: i) the presence of linearly polarized
 245 orographic GWs ($S_- \approx S_+$) or ii) a low total GW energy, where any polarization is possible.

246 Accordingly, for i), NC_R will be close to but different from zero and if ii), any NC_R value may be
247 expected.

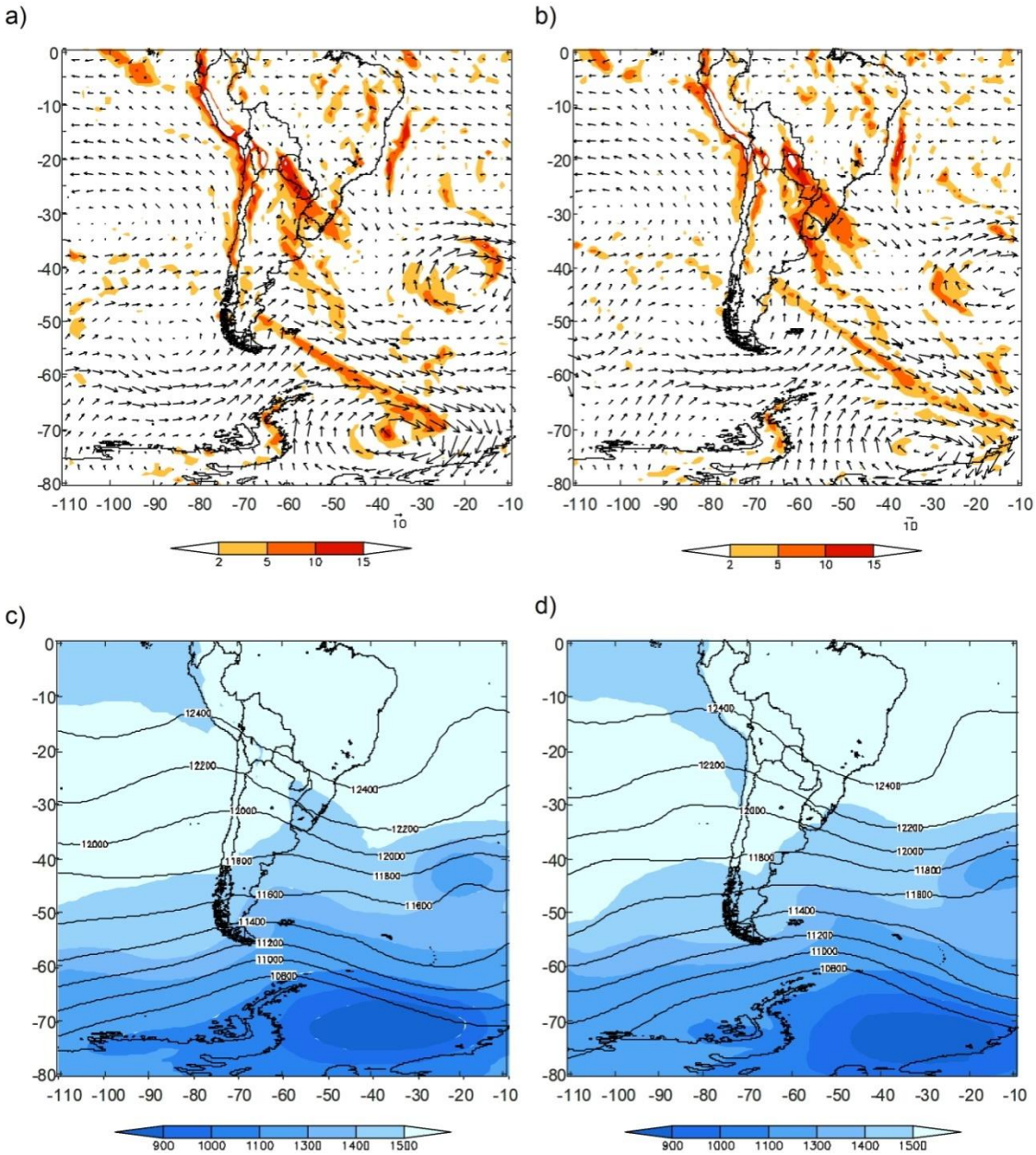
248 **3 IFS model reanalysis and experimental data: a case study**

249 The Integrated Forecasting System (IFS) of the European Centre for Medium-Range Weather
250 Forecasts (ECMWF) is a global, hydrostatic, semi-implicit, semi-Lagrangian model for
251 numerical weather prediction (horizontal resolution: $0.1^\circ \times 0.1^\circ$ (e.g., Polichtchouk et al., 2021)).
252 Perturbations of temperature, zonal, meridional and vertical wind velocity were inferred by
253 subtraction from vertical profiles of T, u, v, w with a low pass cutoff at 15 km. GWs are
254 considered to be well represented in IFS analyses up to an altitude of 55 km (Ehard et al., 2015).
255 At higher altitudes, the simulated wave activity is damped within the model's sponge layer for
256 numerical reasons.

257 The ALIMA lidar system was located onboard the German research aircraft HALO. It yields
258 atmospheric density profiles in the altitude range from 20 to 90 km. T between 20 and 80 km
259 altitude is obtained with varying degrees of accuracy. From 20-60 km, 60-70 km and 70-80 km,
260 the corresponding error is 0.9, 2.9, and 6.5 K respectively. To separate GW induced temperature
261 perturbations from atmospheric background temperatures, a 30 min running mean is applied.

262 The seven HALO flights designed for the study of GW dynamics took off from Río Grande.
263 Each of them travelled along a trajectory typically around 7000 km.

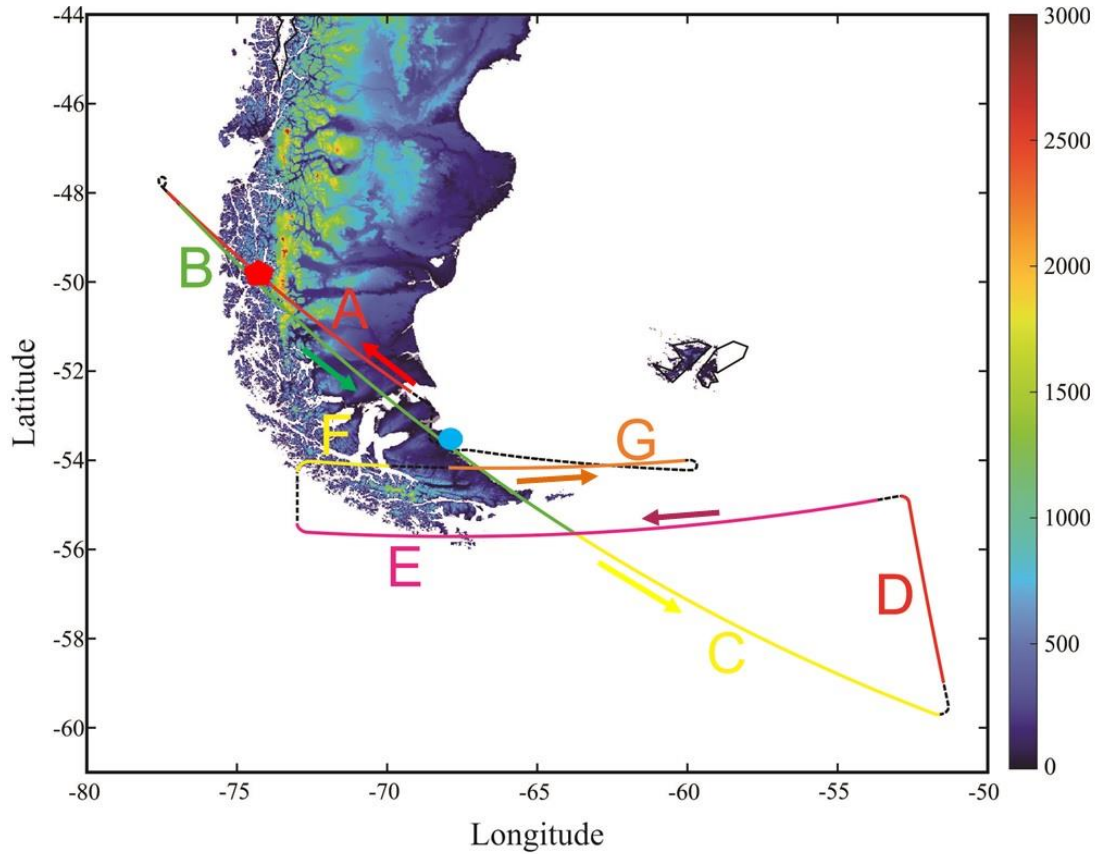
264 The synoptic conditions for Flight 08 were dominated by a sudden stratospheric warming (SSW)
265 that was present during September 2019, as described by Dörnbrack et al (2020). Although it
266 was a weak event (Rapp et al., 2021), it affected the propagation conditions for MWs. In Figure
267 1a, the equivalent potential temperature shows a cold front at 850 hPa around $45\text{-}50^\circ\text{S}$. After 12
268 hours (Figure 1b), the air mass has been displaced to the north leaving the continent at lower
269 levels. At 200 hPa, the streamlines field shows a deepening of the 850 trough with an almost in-
270 phase N-S axis (Figure 1c) with a displacement to the east of the axis of the trough and an almost
271 divergent flow over southern Patagonia (Figure 1d).



272

273 **Figure 1.** Synoptic conditions from NCEP on September 12, 2019. Equivalent potential temperature [K] at a) 00
 274 UTC and b) 12 UTC. Geopotential height [m] at c) 00 UTC and d) 12 UTC. Isolines correspond to 200 hPa and
 275 colorbar to 850 hPa.

276 The trajectory followed by HALO during this flight is shown in Figure 2. Taking into account
 277 the takeoff time and duration of this flight, below we will consider IFS simulations available
 278 within this interval, on 12 September, 00UTC. Six segments (or legs) from this flight may be
 279 identified, on the basis of their lengths and constant direction and pressure levels. The latitude-
 280 longitude coordinates corresponding to the extremities of each leg are provided in Table 1.



281
 282 **Figure 2.** Trajectory of HALO flight ST08 during SOUTHTRAC-GW Mission performed on 11/12
 283 September 2019. The position of the aircraft at 00:00 UTC on 12 September is indicated by the red
 284 pentagon. Seven segments (named from A to G - Table 1), correspond to seven constant pressure altitude
 285 legs followed by HALO. The orographic height is indicated in the colorbar [m]. HALO's takeoff location
 286 at Río Grande is shown by the blue circle.

L eg	Initial latitude	Final latitude	Initial longitude	Final longitude	Static pressure [hPa]	Pressure altitude [Giez et al 2017] [m]	Beginning (min)	End (min)
A	52.47° S	47.99° S	69.20° W	77.31° W	238.3	10670	0	59
B	48.27° S	55.62° S	76.91° W	63.78° W	178.2	12510	69	149
C	55.62° S	59.70° S	63.78° W	51.63° W	178.2	12510	149	201

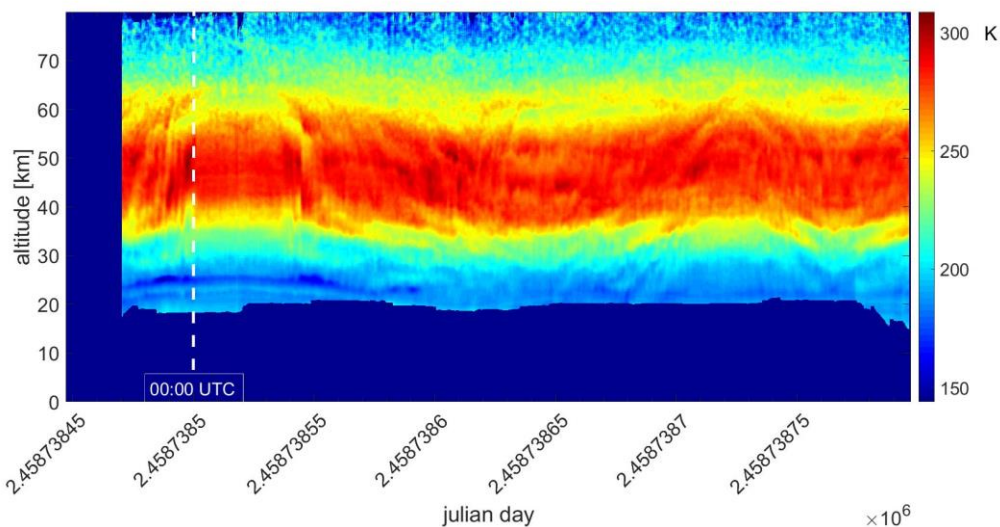
D	58.97° S	54.80° S	51.47° W	52.85° W	161.7	13130	208	245
E	54.89° S	55.42° S	53.66° W	73.00° W	147.1	13740	250	355
F	54.26° S	54.12° S	73.00° W	69.97° W	147.1	13740	363	376
G	54.17° S	54.01° S	67.96° W	60.12° W	133.6	14340	384	415

287

288 **Table 1.** Parameters defining the six constant pressure legs. Leg names A – G are as in Figure 1. Time
 289 intervals (in min) correspond to each leg in Figure 2, counting from the beginning of leg A.

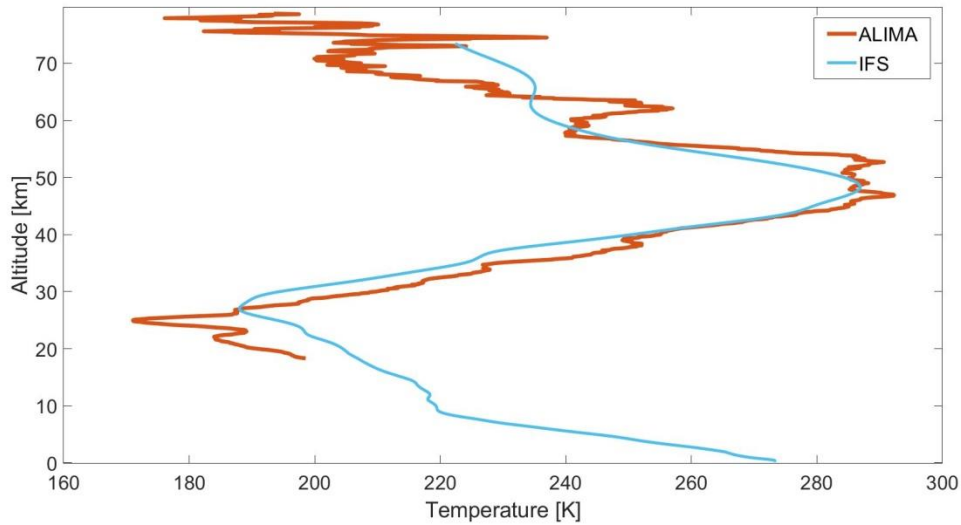
290 The comparison between ALIMA data (resolution 0.9 km) and ECMWF IFS reanalysis on 12
 291 September 00UTC is shown in Figure 3. It shows T as a function of altitude and time as retrieved
 292 from ALIMA during the full flight. The observed general variability mimics the latitude sectors
 293 and synoptic conditions cut across by HALO. The ALIMA T profile at 00UTC exhibits an
 294 intense wave structure up to the mesopause (Figure 3b). A relative agreement is observed in the
 295 stratosphere. The model progressively fails to solve the wavelike structure above 55 km. Note
 296 that experimental vertical profiles of horizontal or vertical wind are not available from this
 297 campaign.

298 a)



299

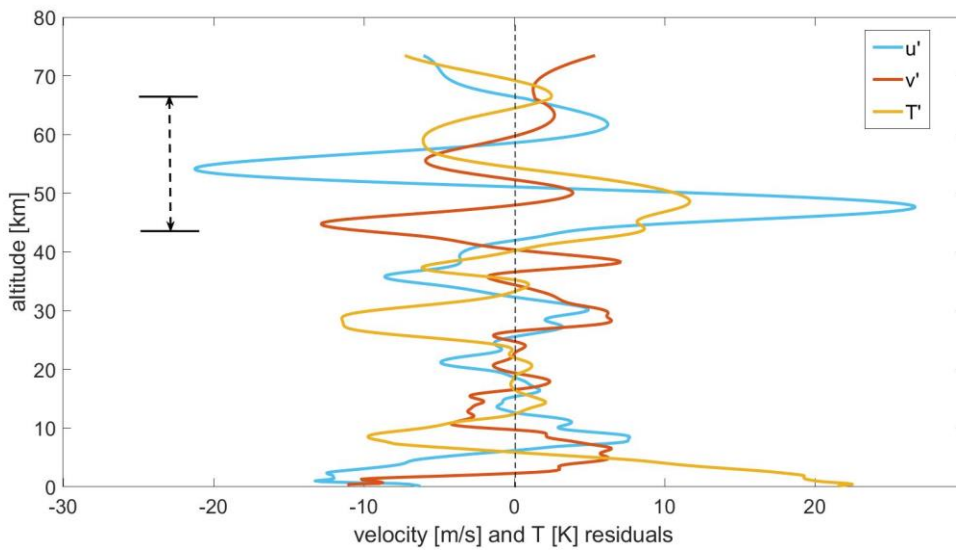
300 b)



301
 302 **Figure 3.** (a) Time-altitude section of temperature retrieved by the ALIMA lidar during flight ST08
 303 along the flight track covering different regions and containng sharp turns as shown in Fig. 2. The dashed
 304 white line marks 0 UT on September 2019 when HALO crossed the highest peak of the southern Andes at
 305 50.01 S and 74.97 E and for which we use IFS reanalysis. (b) IFS and ALIMA T for this time are
 306 compared.

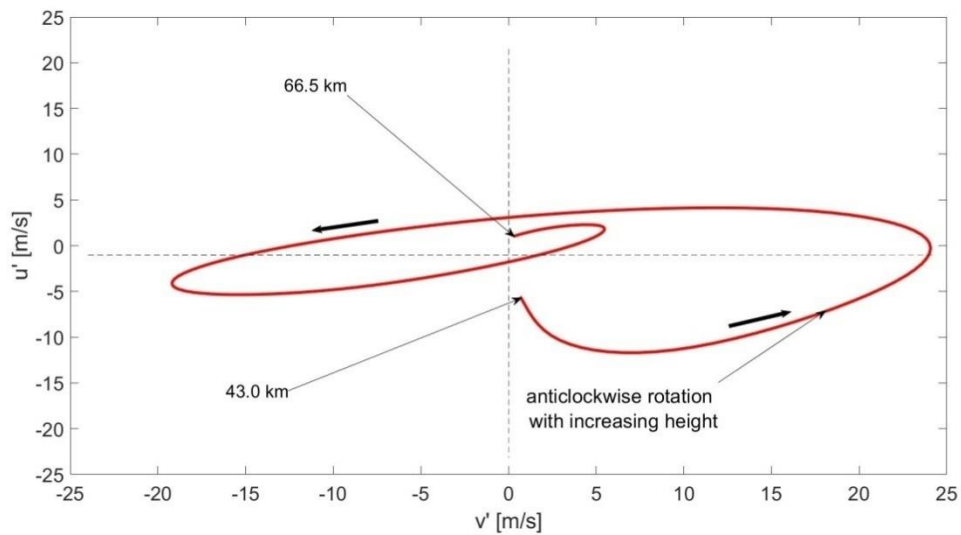
307 Figure 4a show the IFS u' , v' and T' residuals at the 00UTC HALO position at 50.01 S and
 308 73.97 E. A highpass runing mean filter was applied to keep vertical wavelengths below a cutoff
 309 of 15 km in order to retain in the profiles mainly GWs, filtering out possible and non negligible
 310 planetary wave and tide contributions. A general more intense GW activity is observed in the
 311 strato-mesosphere regions compared to lower levels. Note the large amplitude oscillation in the
 312 selected vertical interval. Despite partially exceeding our imposed limit where the sponge begins
 313 at 55 km, the vertical interval between 43.0 and 66.5 km allows to illustrate the classic
 314 hodographic method. In Figure 4b, an anticlockwise rotation of the horizontal velocity
 315 perturbation with increasing altitude is observed in the selected interval. This indicates a
 316 dominant upgoing and probably non-orographic inertia GWpossibly generated close to jet
 317 levels, where the GW amplitude was observed to be considerably smaller.

318 a)



319

320 b)

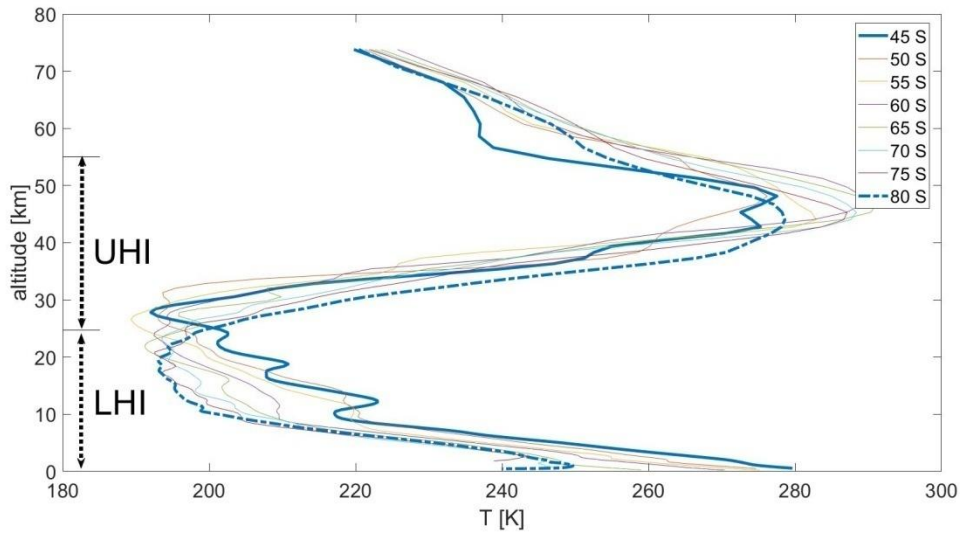


321

322 **Figure 4.** a) Zonal and meridional wind and temperature residuals at 00UTC HALO position (latitude/longitude = -
 323 50.01/-73.97), during ST08 flight on September 12, 2019. A highpass filter for vertical wavelengths below 15 km
 324 was applied. A selected highlighted vertical interval (43.0-66.5 km) is shown. b) Hodograph corresponding to the
 325 vertical interval highlighted in a), showing the anticlockwise rotation with increasing height.

326 From IFS simulations, the detected average coldest height is situated at ~25 km (26 hPa). Here,
 327 the lapse rate changes sign (also in conjunction with the position of the polar night jet core -see
 328 next section-). Then we divide the overall altitude interval below the IFS sponge layer into two
 329 sectors: [0, 25] km and [25, 55] km, namely, lower and upper height intervals (LHI and UHI),

330 respectively. Figure 5 illustrates vertical T profiles from IFS data, at an arbitrary longitude
 331 (70°W), every 5° between 45°S and 80°S . The profiles exhibit typical lapse rates above and
 332 below the ACH in the region considered in this study. The ACH is substantially higher than the
 333 average thermal tropopause, according to the frequent multiple tropopauses structure.



334

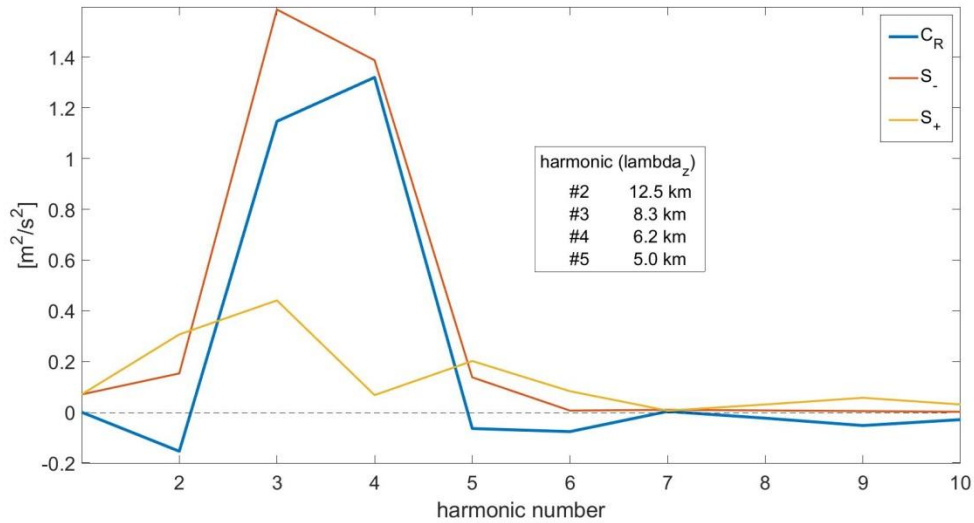
335 **Figure 5.** Vertical T profiles from IFS data at 70°W , every 5° between 45°S and 80°S , exhibiting the typical lapse
 336 rates above and below the ACH in the region considered in this study.

337 **4 SRA at 00UTC on September 12, 2019**

338 **4.1 LHI (Lower Height Interval)**

339 After an interpolation in log-pressure vertical coordinates, a Hanning taper to reduce the spectral
 340 leakage is applied to u' and v' . Following the spectral transformation described in section 2 (eq.
 341 (4) to (10)) C_R , E_T and NC_R are obtained in the position HALO was at 00UTC, 12 September
 342 (flight 08). An altitude column between 0 and 25 km is considered here. C_R (see Figure 6), E_T (= $S_- + S_+$) and NC_R (not shown) exhibit relevant amplitudes only at the first harmonics.

343



344

345 **Figure 6.** Rotary, counterclockwise and clockwise energy coefficient (C_R , S_- and S_+ , respectively) corresponding to
 346 the first 10 harmonics obtained in LHI (between 0 and 25 km height), at the 00UTC HALO position (lat/lon = -
 347 50.01/-73.97) on September 12, 2019, during ST08 flight.

348 Significant rotational energy is distributed between harmonics #2 and #5, which correspond to
 349 vertical wavelengths (λ_z) between 12.5 and 5 km, revealing a clear dominant net upwards flux.
 350 For harmonics larger than #5 ($\lambda_z < 5.0$ km), the remaining rotational energy suddenly decreases
 351 to negligible values. The HALO flight position at the lat/lon pixel corresponding to this figure
 352 lies immediately west of the mountains, not strictly above them. Accordingly, modes with C_R
 353 different from 0 (not LP) suggest a significant GW contribution possibly originated in non-
 354 orographic sources. We may wonder under what conditions the GW energy at any pixel can be
 355 adequately described by only a few modes. The concept of a possible dominant quasi-
 356 monochromatic GW packet at any geographical position seems questionable, at least in the
 357 complex region considered here.

358 We extend the analysis illustrated in a single column (pixel) to the overall latitude-longitude
 359 region, made up by $1001 \times 351 = 351,351$ independent ($0.1^\circ \times 0.1^\circ$) pixels. In doing so, we delimit
 360 our geographic area of interest: [45S-80S, 120E-20E].

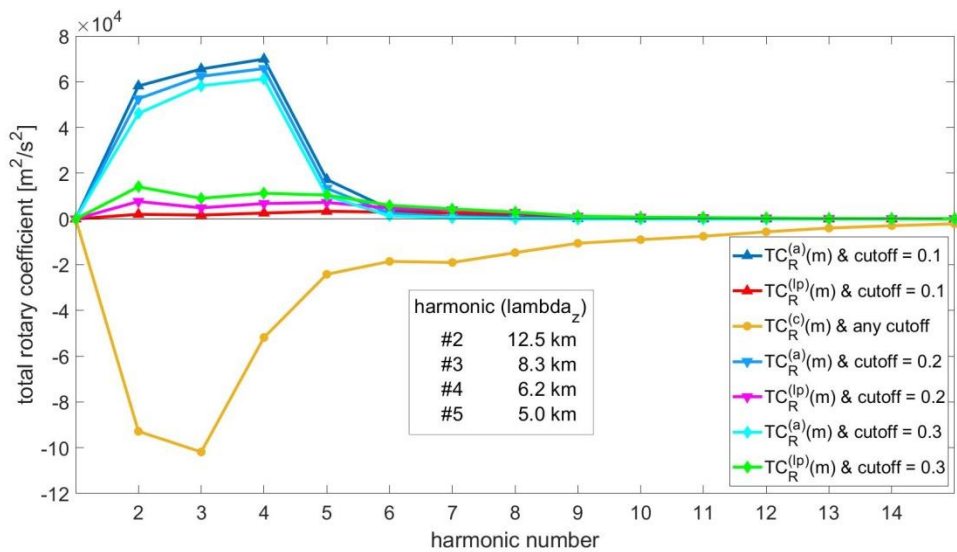
361 We define, for each harmonic, two quantities:

362 1) The total rotary coefficient, $TC_R^{(i)}(m)$, equal to the sum of $C_R(m)$ over all the p_i -pixels. Here, i
 363 = (a) anticlockwise, (lp) linearly polarized or (c) clockwise and $p_a(m) + p_n(m) + p_c(m) = 351,351$

364 pixels, for each m . $TC_R^{(i)}(m)$ may be interpreted as the total up- and downgoing GW energy, as a
 365 function of each vertical wavelength.

366 2) The average rotary coefficient, $AC_R^{(i)}(m) = TC_R^{(i)}(m) / p_i(m)$, that is to say, $TC_R^{(i)}(m)$
 367 normalized over the total number of p_i -pixels. $AC_R^{(i)}(m)$ may be interpreted as the distribution of
 368 GW energy density at each p_i subsector, within the overall geographic domain. For example, we
 369 expect to observe enhanced upgoing GW energy flux concentrated around mountain areas. If we
 370 select any different geographic region, this will modify both $TC_R^{(i)}(m)$ and $AC_R^{(i)}(m)$.

371 According to the criteria we use to distinguish between orographic from non-orographic GWs,
 372 those pixels with $C_R(m)$ lying close to 0 are identified as LP. The “closeness” of $C_R(m)$ to 0 for a
 373 given m is, of course, arbitrary. To isolate LP GWs, we may choose, for example, upper and
 374 lower C_R thresholds as $[-\alpha, +\alpha] m^2/s^2$, where $0 < \alpha \ll 1$. However, GWs from orographic origin
 375 are expected to be LP and, in addition, upgoing. Then, we propose that C_R must be > 0 and we
 376 set the upper and lower thresholds: $[0, +\alpha] m^2/s^2$. To illustrate the variability arising from these
 377 constraints, in Figure 7 we show $TC_R^{(i)}(m)$ for the first 15 harmonics and three arbitrary upper
 378 thresholds: $\alpha = 0.1, 0.2$ and 0.3 .



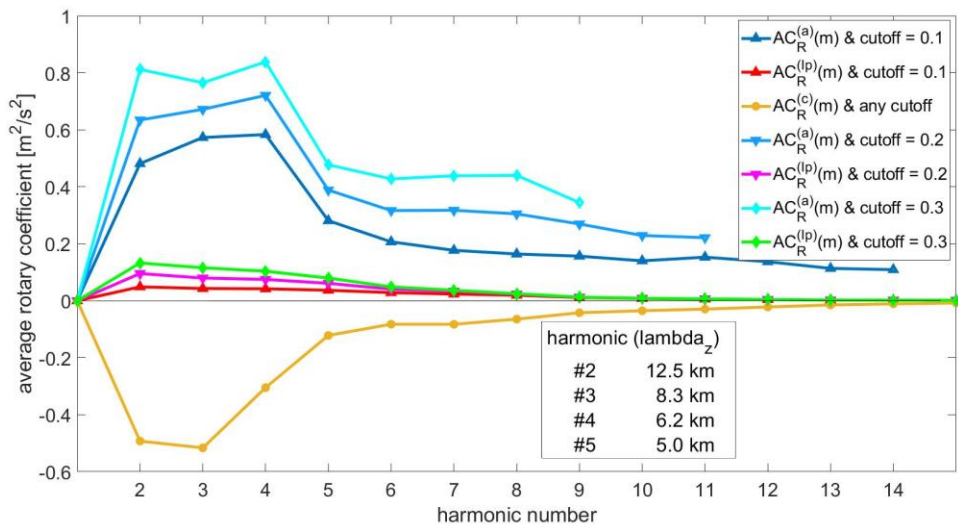
379

380 **Figure 7.** Total rotary coefficient, $TC_R^{(i)}$, calculated in the overall latitude-longitude region, made up by
 381 $1001 \times 351 = 351,351$ ($0.1^\circ \times 0.1^\circ$) pixels. $i = (a)$ anticlockwise, (lp) linearly polarized or (c) clockwise GW rotation.
 382 Three cutoffs defined to distinguish between GWs of orographic and non orographic sources are arbitrarily chosen
 383 to show the variability of each upgoing contribution to the overall energy flux. According to our definition, different
 384 upper cutoffs do not affect downgoing GWs.

385 Some features may be noted:

- 386 • The main energy flux is concentrated in the lower harmonics. A fast decrease in $TC_R^{(a)}$
- 387 with increasing m reveals an accumulation of GW energy only in this spectral range. A
- 388 net larger downgoing energy flux is observed above the overall geographic sector
- 389 considered here. At first glance, this result may be somehow unanticipated, if we do not
- 390 take into account that most of the region is covered by oceanic areas, in comparison to
- 391 mountain regions.
- 392 • $TC_R^{(c)}$ corresponding to downgoing GW rotational energy flux, in turn, diminishes with m
- 393 considerably slower. This energy is spread into additional shorter vertical wavelengths
- 394 than $TC_R^{(a)}$. It is unaffected by the variability in the upper cutoff.
- 395 • Downwards GW energy flux distribution among larger m values suggest a possible
- 396 relevance of inertia GWs, generated after geostrophic imbalance close to or at polar night
- 397 jet levels. In addition, reflection effects may be significant.
- 398 • $TC_R^{(a)}$ ($TC_R^{(lp)}$) decreases(increases) with increasing(decreasing) upper cutoff. We remind
- 399 that these two parameters share the total available upgoing energy flux.

400 In Figure 8, we show the $AC_R^{(i)}$ distribution.

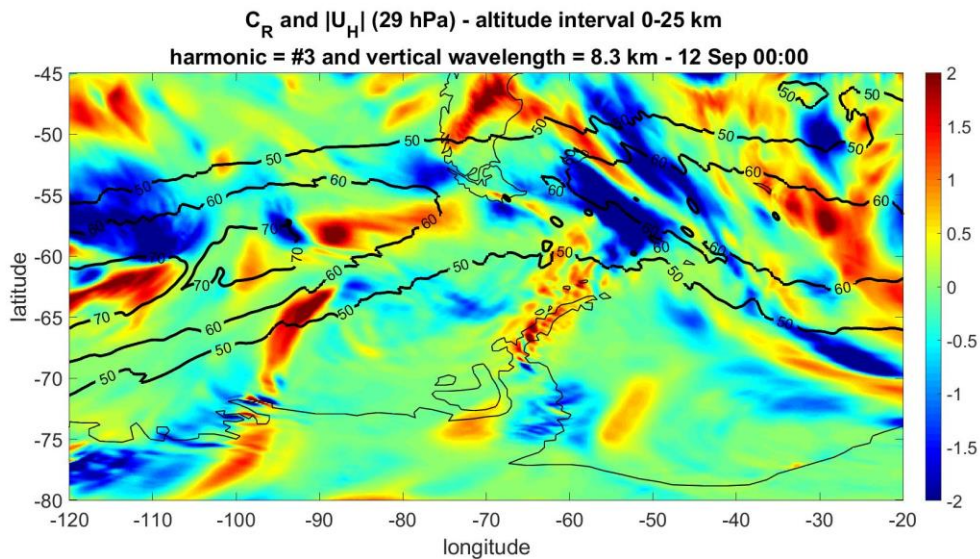


401
402 **Figure 8.** Average rotary coefficient, $AC_R^{(i)}$, calculated in the latitude-longitude region as in Figure 7.

403 The following features can be observed:

- 404 • The relative relevance of upgoing as compared to downgoing GW energy per unit area is
 405 now evident. Clearly, it is concentrated in limited subregions, mostly corresponding to
 406 mountain areas. These are defined by a considerably lower pixels number than those
 407 corresponding to downgoingGWs.
- 408 • $AC_R^{(a)}$ is here always larger than $AC_R^{(c)}$ and increases with increasing upper cutoff,
 409 inversely to what is observed when comparing $TC_R^{(a)}$ and $TC_R^{(c)}$. $AC_R^{(lp)}$ increases with
 410 increasing upper cutoff, similarly to what happens with $TC_R^{(lp)}$.
- 411 • As the cutoff is set to larger values, p_a is equal to zero beyond a given harmonic and
 412 $AC_R^{(a)}$ is obviously not defined. For these higher cutoffs, the total available upgoingGW
 413 energy flux seems to be shared only between a few harmonics.
- 414 • The enhance of $AC_R^{(lp)}$ with increasing cutoff, also observed in $TC_R^{(lp)}$, suggests that the
 415 number of pixels defining the total area with LP GWs seems not to expand significantly.
 416 These are are concentrated in reduced areas.

417 In Figure 9 we analyze the geographic distribution of $C_R(m)$, now in a latitude-longitude plot.
 418 For illustrative purposes, we first perform an approximation of the general characteristics that
 419 can be extracted from this parameter. We select one representative dominant harmonic (#3),
 420 based on the results in Figure 8. This harmonic corresponds to $\lambda_z = 8.3$ km. The plot was
 421 obtained at 00UTC, on 12 September 2019.

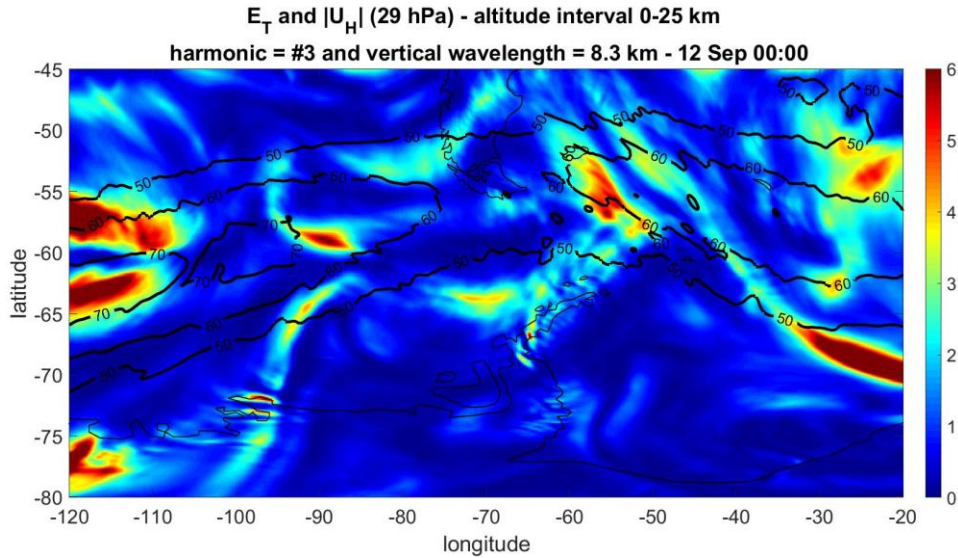


423 **Figure 9.** Rotary coefficient for harmonic #3 in [m^2/s^2], corresponding to $\lambda_z = 8.3$ km. The black isolines show the
 424 absolute value of the horizontal wind in [m/s] at 29 hPa, where the core of the polar night jet is found.

425 We interpret the different pixel regions as follows. Positive(negative) C_R values correspond to
 426 GW packets with dominant anticlockwise(clockwise) rotation with increasing height. This is
 427 what is expected from upwards(downwards) energy propagation in the southern hemisphere.
 428 Pixels with C_R bounded between 0 and α with $\alpha \ll 1$ indicate subregions where one of two
 429 possible characteristics prevails: dominant LP, as expected from typical MWs (as explained
 430 before, we consider only $\alpha > 0$), or with negligible GW activity. This uncertainty may be
 431 removed by plotting E_T (m) for the same #3 harmonic (see below). The position of the jet core
 432 (black contours) is situated above oceanic and continental areas at 25 km height (26 hPa). Some
 433 features can be identified from this figure, bearing in mind that it corresponds only to a single
 434 harmonic:

- 435 • Two subregions with upwards propagating GW energy above continental areas over
 436 central Patagonia and the Antarctic Peninsula show different degrees of elliptic
 437 polarization.
- 438 • Above southern Patagonia and Tierra del Fuego Island, there is a predominance of LP
 439 GWs, suggesting their orographic origin.
- 440 • Above the remaining oceanic areas, there is a broad distribution of up- and downgoing
 441 energy flux. In particular, at and near to the jet and the jet streak position. As mentioned
 442 before, possible sources for this variability may be found in departures from geostrophic
 443 equilibrium near to the jet and the proximity to the cold front.

444 In Figure 10 we show E_T also for #3:



445

446 **Figure 10.** Total rotary energy for harmonic #3 in $[m^2/s^2]$, corresponding to $\lambda_z = 8.3$ km. The black isolines show
447 the absolute value of the horizontal wind in $[m/s]$ at 29 hPa, where the core of the polar night jet is found.

448 The following features are observed:

- 449
- 450 • A geographic correspondence between subregions where E_T is enhanced and extreme C_R
451 values (Figure 9). This is seen mostly near to the jet (Figure 10).
 - 452 • This feature also applies to central Patagonia and the Antarctic Peninsula, although with
453 less intense E_T values than near the jet stream. Taking into account that the characteristics
454 observed in figures 9 and 10 are very different for any different m , in videos 1 and 2 we
455 extend the description of figures 9 and 10 respectively, as a function of m between #2 and
456 #6. The distributions of C_R and E_T are shown. Equal scales were preserved within each
457 video, for comparison. There is a general increasing variability with increasing m of the
458 up- and downgoing structures. This provides an insight of the complex GW ensemble to
be expected in the region considered here.
 - 459 • The geographic distribution of the enhanced C_R subregions is different for each harmonic.
460 The same is observed for subregions where LP GWs are expected.
 - 461 • The opportunity of isolating geographic sub-regions where monochromatic waves would
462 dominate seems unrealistic.
 - 463 • The overall amplitude of C_R decreases with increasing m , as expected from the features
464 in Figure 7.

- 465 As in the case of C_R , the geographical distribution of sub-regions of enhanced E_T is

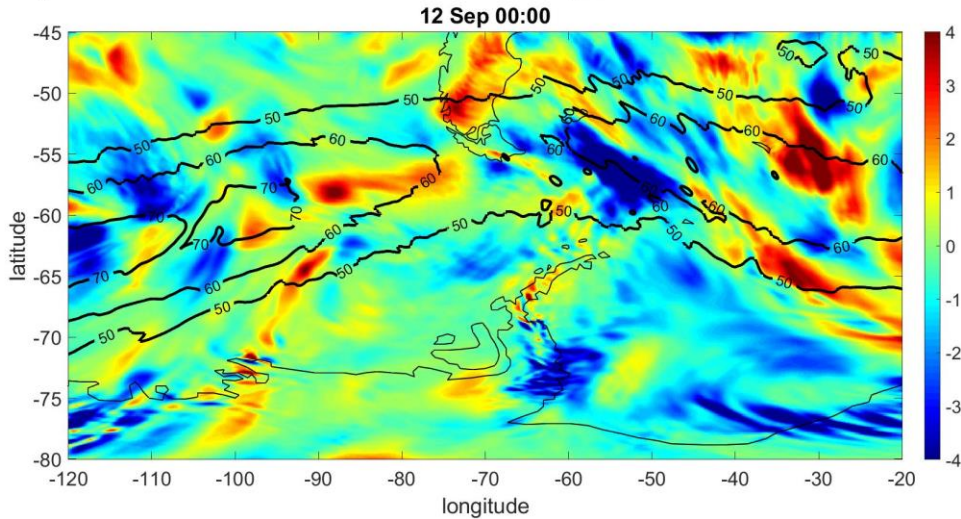
466 different for each m . An overall decrease in E_T with increasing m is also evident. To

467 better appreciate the cumulative effect through m of C_R and E_T , in Figures 11 and 12

468 these parameters are added over the whole set of harmonics, namely, $C_{R(INT)}$ and $E_{T(INT)}$,

469 respectively. Note that these figures were rescaled with respect to Figures 9 and 10.

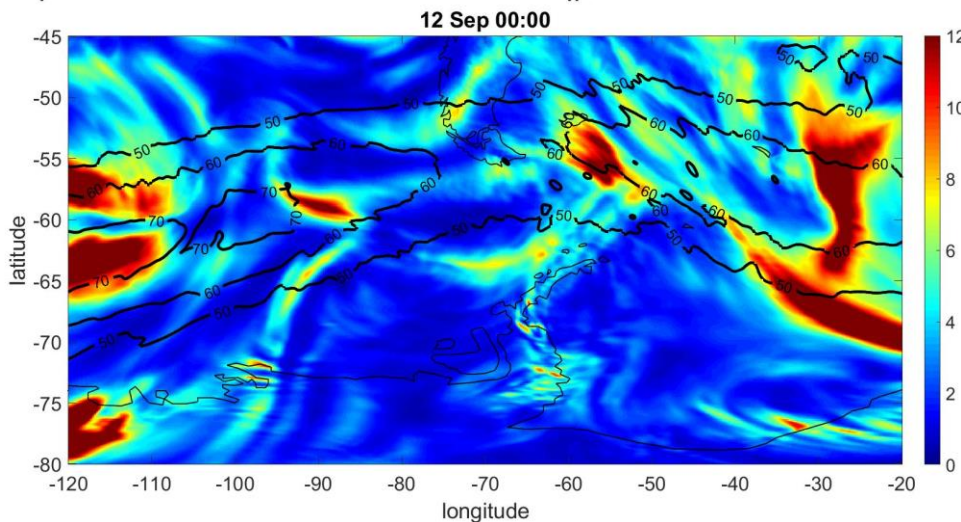
C_R integrated over the whole set of harmonics and $|U_H|$ (29 hPa) - altitude interval 0-25 km



470

471 **Figure 11.** $C_{R(INT)}$, in $[m^2/s^2]$, obtained by adding all the harmonics $C_R(m)$.

E_T integrated over the whole set of harmonics and $|U_H|$ (29 hPa) - altitude interval 0-25 km

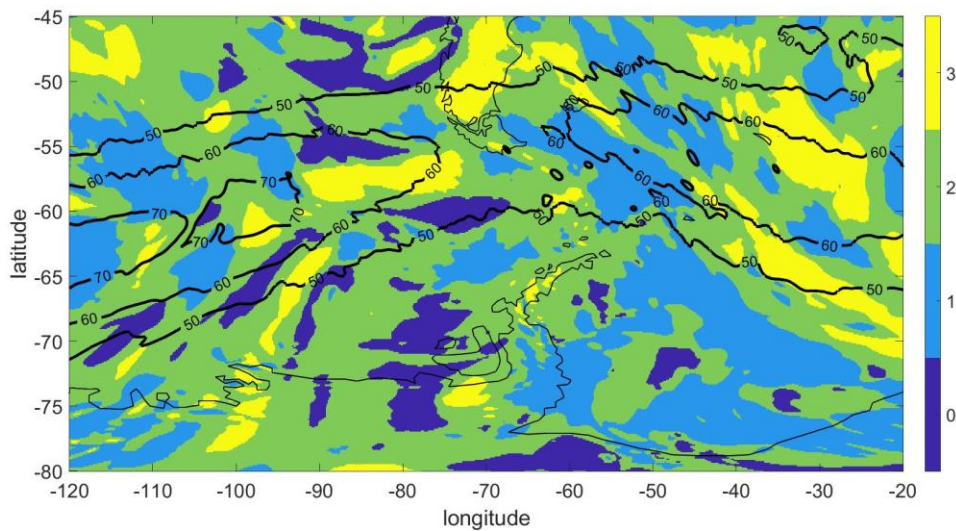


472

473 **Figure 12.** $E_{T(INT)}$, in $[m^2/s^2]$, obtained by adding all the harmonics $E_T(m)$.

474 In addition to the general characteristics already described, near the jet, a high concentration of
 475 GW energy with a significant degree of non-linear polarization is evident, especially over
 476 oceanic areas.

477 In Figure 13, we classify the distributions from Figures 11 and 12 in four groups as follows: GW
 478 packets with i) negligible total wave energy, ii) anticlockwise rotation, iii) mainly LP and iv)
 479 clockwise rotation. We label each of these 4 groups with an index "0", "1", "2" or "3"
 480 respectively. Sub-regions where the total wave energy remains below an arbitrarily cutoff $C = 1$
 481 m^2/s^2 (group i), we assign an index "0". If the energy is greater than C , we assign an index "1"
 482 or "3", for C_R negative or positive, respectively. Finally, we assign "2" if C_R lies within the
 483 interval $[0, +r]$ (after Figures 7 and 8, for brevity we only illustrate with $r = 0.3 \text{ m}^2/\text{s}^2$). We
 484 interpret this last group as containing the dominant LP GW packets.



485
 486 **Figure 13.** The four areas with different up- and downgoing dominated GWs. Labels "0", "1", "2" and "3", indicate,
 487 respectively, C_R values with negligible total rotational energy, downgoing dominated GW energy flux, LP and
 488 upgoing. Here $C = 1 \text{ m}^2/\text{s}^2$ and $r = 0.3 \text{ m}^2/\text{s}^2$.

489 The following features may be noted:

- 490 • Upgoing GW energy flux subregions ("3") (or pixel groups) are mostly situated above
 491 Patagonia, Antarctic Peninsula and several oceanic sectors. The latter alternate with
 492 subregions dominated by LP GWs ("2").

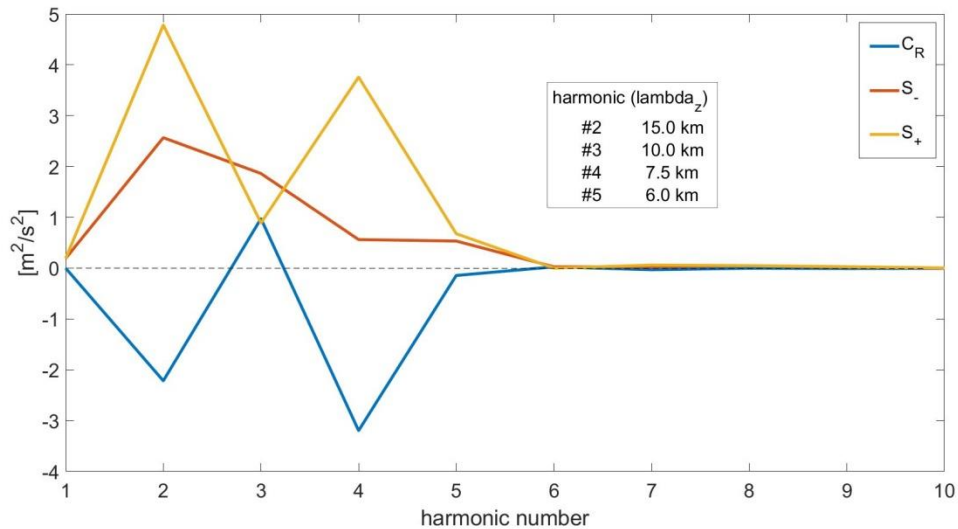
- 493 • The downstream GW sectors ("1") only appear above the sea. As mentioned above, they
 494 represent the main contribution in terms of relative areas (but not in terms of relative
 495 energy flux contribution, as explained after Figure 8) of the overall region under
 496 consideration.
- 497 • For any value of C , the relative coverage of zones "2" and "3" obviously still depends on
 498 r , although, the sum of the two remains unchanged. For example, if we set $r = 0.1$ (figure
 499 8), region "2" will decrease considerably and "1" will increase. If C is modified, the
 500 relative distribution of the 4 regions will also change.

501 In video 3, we show the evolution through successive m values of the normalized rotary
 502 coefficient (NC_R). Clearly, the horizontal spatial scale of variability of this relative
 503 dimensionless coefficient, which is bounded by -1 and $+1$, considerably increases with m . The
 504 complex structure of the different wave packets becomes more evident here than in C_R and E_T . It
 505 must be remarked that the information available from the 3 coefficients, C_R , E_T and NC_R is, in
 506 some sense, complementary. For example, let us consider extreme values: if NC_R is 1 or -1 we
 507 do not know whether the upward or downward rotational energy flux is large or small. This
 508 knowledge is provided by C_R or E_T . On the other hand, if NC_R is close to 0 , from C_R alone no
 509 information about E_T is available. However, in this case from NC_R we infer that the energy flux
 510 associated to the presumed LP mountain waves is significant. In video 3, this occurs in the
 511 transition zones between red and blue sectors. Nevertheless, it must be remarked that the
 512 conclusions drawn from each image are valid only for its corresponding harmonic.

513 **4.2. UHI (Upper Height Interval)**

514 Following the procedure applied in section 4.1, we now consider the interval $[25, 55]$ km. Note
 515 that instead of the simple separation proposed here between LHI and UHI, other spectral
 516 intervals could also reveal significant features and possible sources, e.g. a sliding vertical
 517 window or non overlapping vertical intervals with different lengths. We expect that the coercive
 518 presence of the jet may provide a "turning point" in the net vertical energy flux. Regions where
 519 geostrophic unbalance exists near to the jet may constitute a non negligible GWs source. In the
 520 absence of critical layers, orographic GWs may also be able to propagate high in the
 521 stratosphere; hence, we expect that the two main sources of upgoing GWs are the same as in
 522 LHI. Figures 14 to 21 represent, respectively, the counterparts of Figures 6 to 13 in UHI.

523 On the basis of the description already made in the previous section, in UHI, the relevant
 524 similarities with and differences from the lower levels are detailed below each figure.

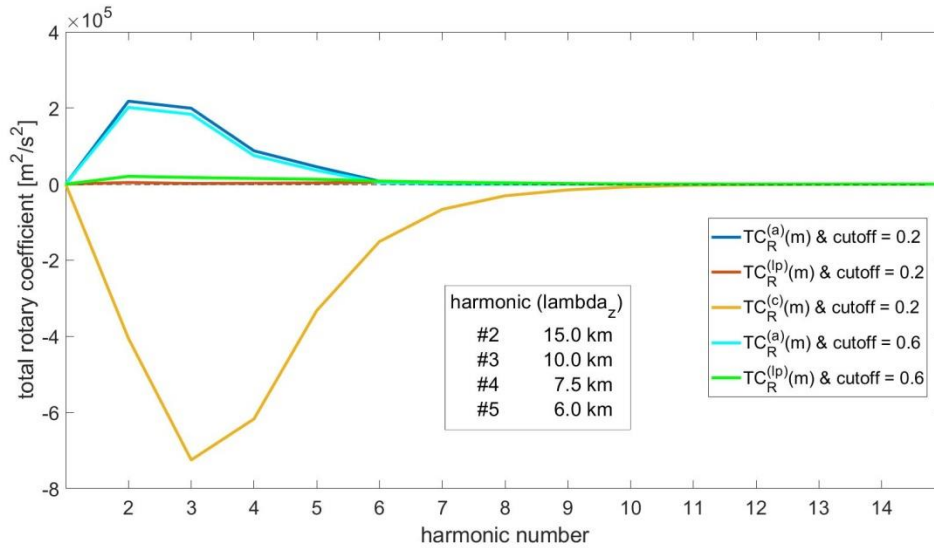


525

526 **Figure 14.** As in Figure 6, rotary, counterclockwise and clockwise energy coefficient corresponding to the first 10
 527 harmonics obtained in UHI (between 25 and 55 km height), at the 00UTC HALO position.

528 In Figure 14, the significant rotational energy in UHI at the single pixel corresponding to the
 529 00UTC HALO position (lat/lon = -50.01/-73.97) on September 12, 2019, during ST08 flight is
 530 shown. It is distributed within the first harmonics, mainly #2 and #4. These correspond to λ_z
 531 equal to 15.0 and 7.5 km, but, in UHI, they reveal a net downwards flux. For harmonics larger
 532 than #5, the remaining rotational energy decreases to negligible amplitudes. As in LHI, C_R
 533 different from 0, suggests that a significant GW contribution originated in non-orographic
 534 sources or that reflection occurred. For #3 ($\lambda_z = 10.0$ km) C_R close to 0 may correspond to an
 535 orographic mode.

536 In Figure 15, identical remarks to those after Figure 7 can be made. The effect of only two
 537 arbitrary cutoffs in the energy flux distribution is shown for illustration.

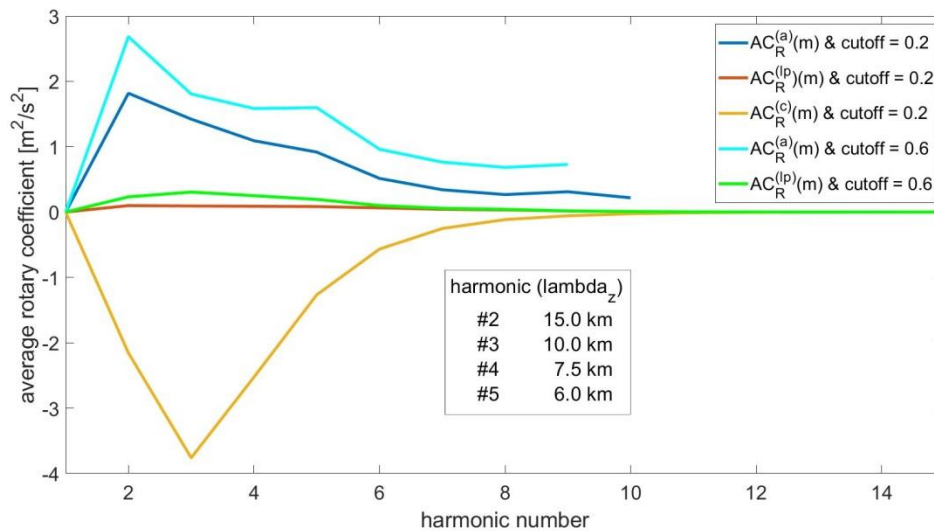


538

539 **Figure 15.** As in Figure 7, $TC_R^{(i)}$ is shown in the overall latitude-longitude region, between 25 and 55 km height.
 540 Here, the effect of two cutoffs is shown.

541 In Figure 16, we now show the $AC_R^{(i)}$ distribution. It can be observed that, contrary to what
 542 happens in LHI, the average upgoing GW energy flux is weaker than the downgoing flux, even
 543 though it is probably concentrated in limited mountainous regions.

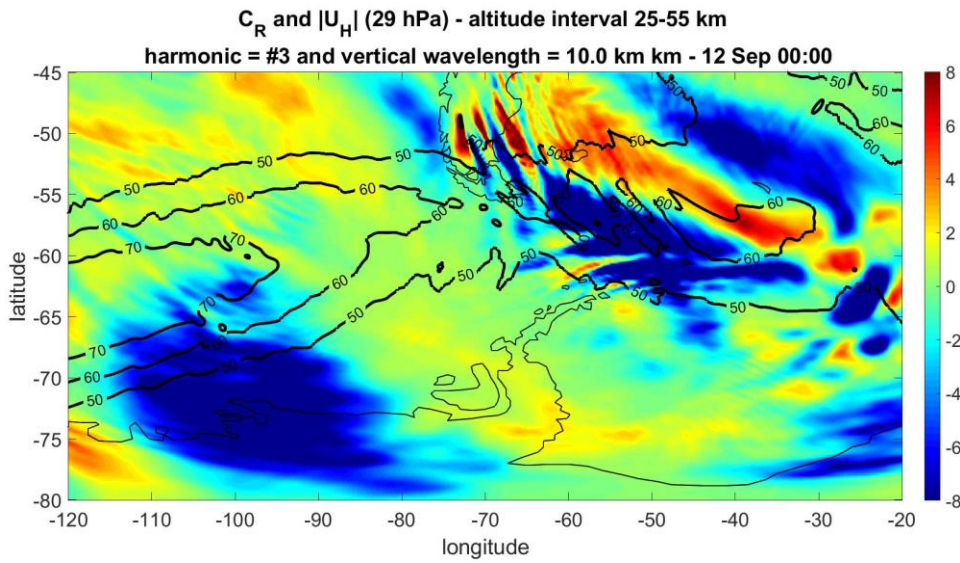
544



545

546 **Figure 16.** Average rotary coefficient, $AC_R^{(i)}$, calculated in the latitude-longitude region as before. The effect of two
 547 cutoffs is shown.

548 In Figure 17, we analyze the geographic distribution of $C_R(m)$ in a latitude-longitude plot,
 549 selecting one representative dominant harmonic (#3), as in Figure 9. This harmonic corresponds
 550 to λ_Z equal to 8.3 km. The plot was rescaled, taking into account that C_R (and E_T below in Figure
 551 18) are in units of energy per unit mass. These magnitudes are expected to increase in the
 552 stratospheric altitudes due to the decrease in air density.



553

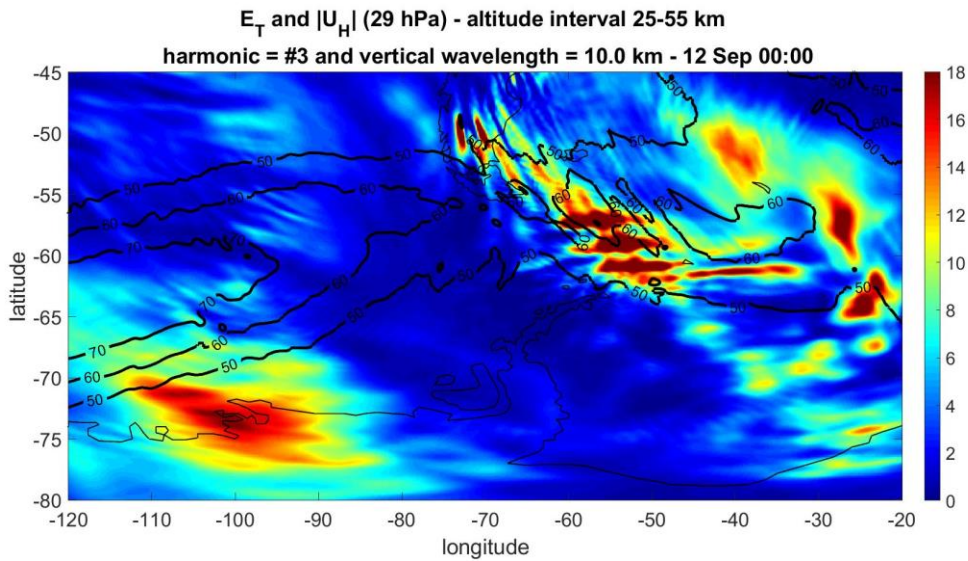
554 **Figure 17.** Rotary coefficient for harmonic #3 in $[m^2/s^2]$, corresponding to $\lambda_Z = 10.0$ km. The black isolines show
 555 the absolute value of the horizontal wind in $[m/s]$ at 29 hPa, where the core of the polar night jet is found.

556 Following the general considerations stated above for Figure 9, we interpret the different regions
 557 in Figure 17 as follows: positive(negative) C_R values correspond to GW packets with dominant
 558 anticlockwise(clockwise) rotation with increasing height. This is what is expected from
 559 upwards(downwards) energy propagation in the southern hemisphere. Pixels with $0 < C_R < \alpha \ll 1$
 560 indicate subregions where one of two possible characteristics prevails: dominant LP, as expected
 561 from typical MWs (as explained before, we consider only $\alpha > 0$), or with negligible GW activity.
 562 This uncertainty may be removed by plotting $E_T(m)$ for the same #3 harmonic (Figure 18). The
 563 position of the jet core (black contours) is situated above oceanic and continental areas at 25 km
 564 height (26 hPa). From this figure:

- 565 • Two subregions with upwards propagating GW energy above continental areas of central
 566 Patagonia and the Antarctic Peninsula, showing different degrees of elliptic polarization.

- 567 • Above southern Patagonia and Tierra del Fuego Island, a predominance of LP GWs is
 568 clear, suggesting an orographic origin.
- 569 • Above the remaining oceanic areas, there is a broad distribution of up- and downgoing
 570 energy flux, in particular at and near to the jet and the jet streak position. As mentioned
 571 before, possible sources for this variability may be found in departures from geostrophic
 572 equilibrium near to the jet.

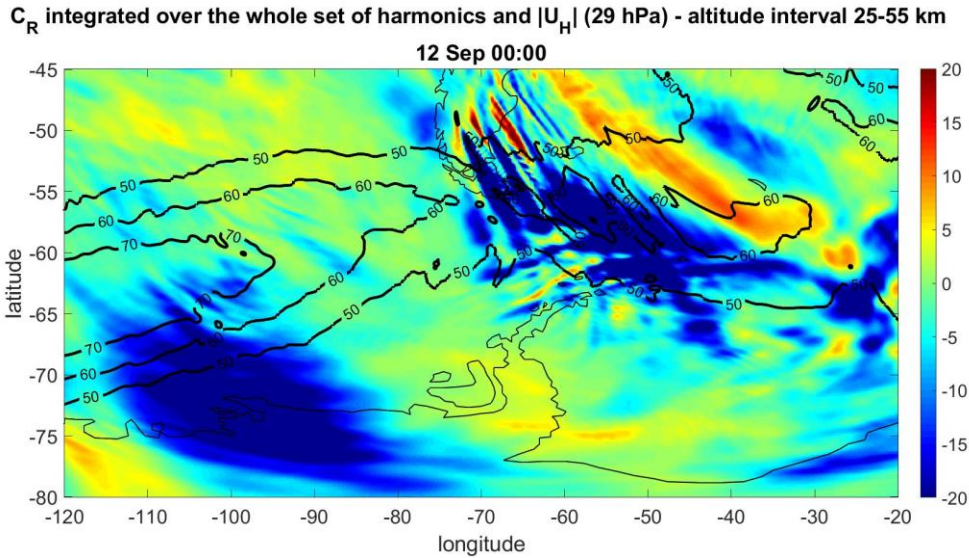
573



574

575 **Figure 18.** Total rotary energy for harmonic #3 in $[m^2/s^2]$, corresponding to $\lambda_z = 10.0$ km. The black isolines show
 576 the absolute value of the horizontal wind in $[m/s]$ at 29 hPa, where the core of the polar night jet is found.

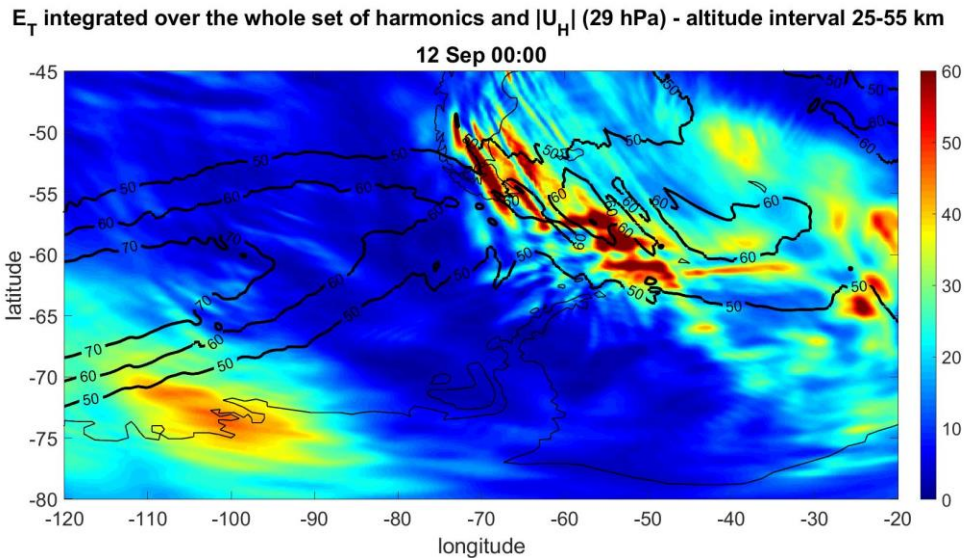
577 The cumulative effect through m , of C_R and E_T in UHI ($C_{R(INT)}$ and $E_{T(INT)}$) is shown in Figures
 578 19 and 20. The regions where upward and downward flows with significant departures from
 579 linear polarization are observed to the east of 70W meridian and in the South Pacific. This is also
 580 observed in E_T .



581

582 **Figure 19.** C_R (INT), in $[m^2/s^2]$, obtained by adding all the harmonics C_R (m).

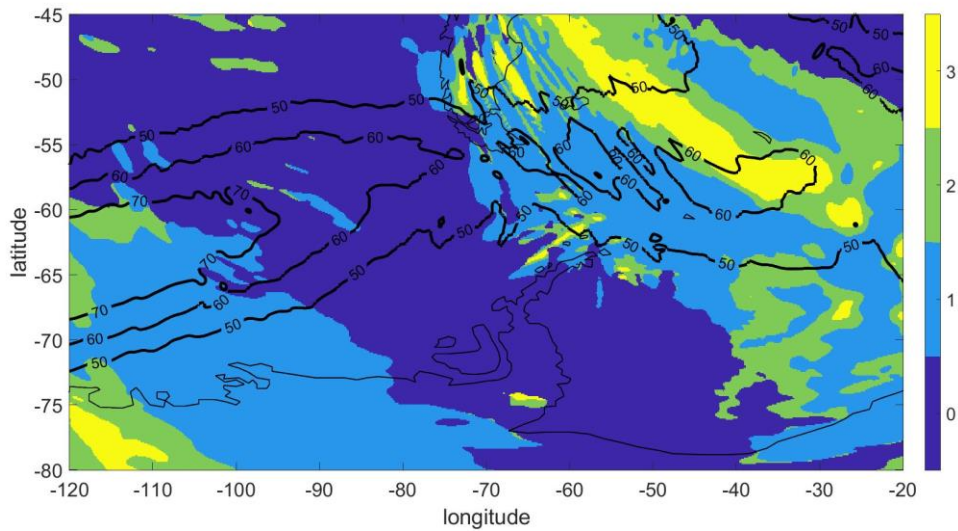
583 In Figure 20, it may be observed that in UHI, the total available GW energy per unit mass is, on
584 average, around five times larger than in LHI.



585

586 **Figure 20.** E_T (INT), in $[m^2/s^2]$, obtained by adding all the harmonics E_T (m).

587 In Figure 21, thresholds $C = 10.0 m^2/s^2$ and $r = 4.0 m^2/s^2$ are adapted to the energy distribution
588 now observed in UHI.



589

590 **Figure 21.** As in Figure 13, the four areas with different up- and downgoing dominated GWs. Labels “0”, “1”, “2”
 591 and “3”, indicate, respectively, C_R values with negligible total rotational energy, downgoing dominated GW energy
 592 flux, LP and upgoing. Here $C = 10.0 \text{ m}^2/\text{s}^2$ and $r = 4.0 \text{ m}^2/\text{s}^2$.

593 We can observe sub-regions with different degrees of polarization where downward flows
 594 dominate, systematically distributed in elongated bands. These are of different widths and have a
 595 predominantly NW-SE direction. Their relative distribution depends, as in LHI, on the arbitrary
 596 choice of r and C cutoffs.

597 Finally, for completeness, we include videos 4 to 6, which are respectively UHI counterparts of
 598 videos 1 to 3. We recall that the characteristics and conclusions drawn from each image shown in
 599 each of the videos 1 to 6 are valid only for the corresponding harmonic and are notably different
 600 for the rest of the harmonics.

601 **5 A comparison with a GW temperature-vertical wind phase difference based analysis**

602 We corroborate our rotational analysis with an independent technique that also allows us to
 603 investigate the upward or downward direction of wave energy propagation. This alternative
 604 analysis was based on the same ECMWF IFS operational analysis data for 12 September 2019,
 605 00:00 UTC, as the rotational analysis introduced above. A brief description of the alternative
 606 technique is given below.

607 ECMWF data was processed using small-volume few-wave decomposition method S3D
 608 (Lehmann et al., 2012), currently implemented as part of the JUWAVE package for GW analysis

609 developed in ForschungszentrumJülich. S3D uses least-squares fitting to determine the
 610 amplitude, 3-D wave vector and phase of several highest amplitude waves in a relatively small
 611 rectangular box (boxes measured 300 km by 300 km in horizontal and 6 km in the vertical
 612 direction in this study). S3D was used to independently find waves (harmonic disturbances) in
 613 temperature and vertical wind data. If both temperature and wind disturbances were indeed a
 614 consequence of GW activity, their phases and amplitudes must satisfy certain conditions that can
 615 be derived from linear GW theory. Following, for example, Section 2.1 of Fritts & Alexander
 616 (2003), one can describe GWs as linear disturbances on a hydrostatic main state satisfying WKB
 617 (Gill, 1982) conditions. Temperature and vertical wind disturbances with amplitudes and phases
 618 T_A , Φ_T and w_A , Φ_w can then be written as

$$619 \quad T = T_A e^{z/2H} \cos(kx + ly + zm - \omega t + \Phi_T) \quad (11)$$

$$620 \quad w = w_A e^{z/2H} \cos(kx + ly + zm - \omega t + \Phi_w) \quad (12)$$

621 where (k, l, m) is the 3-D wave vector, t is time, ω is the wave frequency and H is the scale
 622 height. We also assume that speed of sound is very large, to eliminate acoustic waves from the
 623 analysis. Then, it follows from equation (18) in Fritts & Alexander that $\Phi_T - \Phi_w$ is $\pi/2$ for
 624 upward propagating waves, $-\pi/2$ for downward propagating waves and

$$625 \quad \frac{T_A}{w_A} = \frac{T_0 N^2}{g \omega} \quad (13)$$

626 where T_0 is the undisturbed air temperature, N is the Brunt-Väisälä frequency, g is gravitational
 627 acceleration and ω is the intrinsic frequency of the wave (it can be obtained from the GW
 628 polarization relations knowing k, l, m from wave fit). These relations were used to determine
 629 whether each S3D fitting box contained GWs and whether they were propagating upwards or
 630 downwards. In particular, box was said to contain a GW if either $|\Phi_T - \Phi_w - \pi/2| < 0.2$ (upward
 631 propagating wave) or $|\Phi_T - \Phi_w + \pi/2| < 0.2$ (downward propagating wave) and

$$632 \quad \frac{T_0 N^2}{2g\omega} < \frac{T_A}{w_A} < 2 \frac{T_0 N^2}{g\omega} \quad (14)$$

633 i.e. T_A/w_A was between half and twice the theoretically predicted value.

634 S3D wave fits are most reliable when horizontal and vertical wavelengths of the detected wave
 635 are between about one third of the fitting box size and three fitting box sizes in the respective
 636 direction. Therefore, we only considered GWs with horizontal wavelengths between 100 km and
 637 900 km and vertical wavelengths from 2 km to 18 km.

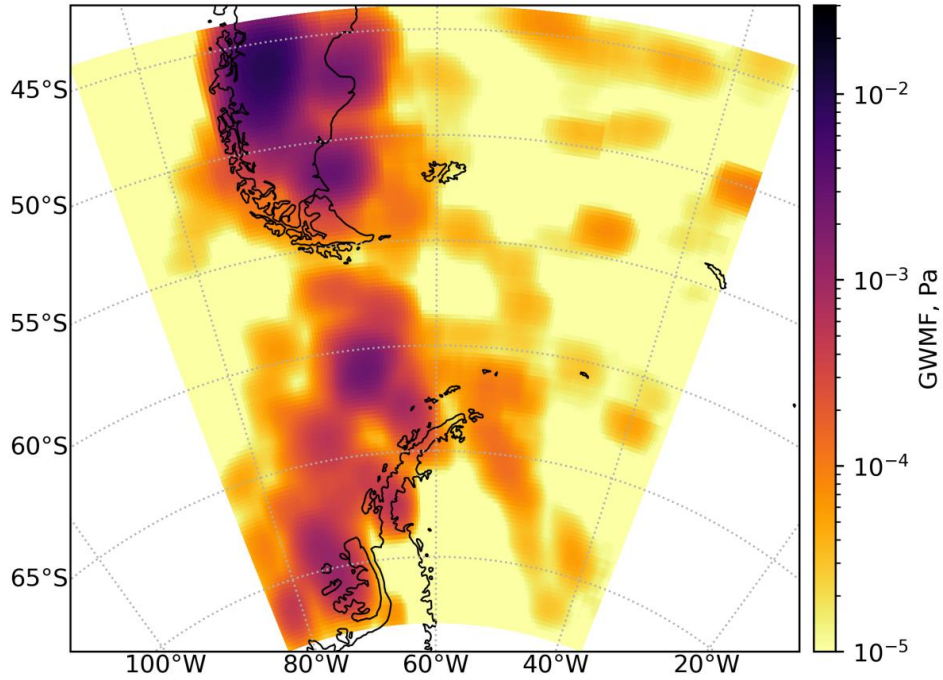
638 To compare this method to rotational analysis, gravity wave activity in a relatively large altitude
 639 range (LHI and UHI intervals) has to be quantified. It is evident from equations (11) and (12)
 640 that the amplitudes T_A and w_A grow exponentially with altitude. Hence, calculating mean
 641 amplitudes over a tall vertical column would almost entirely represent wave activity at the top of
 642 the column. To avoid this problem, we will quantify the amount of wave activity using the
 643 density of flux of the horizontal momentum (gravity wave momentum flux; GWMF)

$$644 \quad F = \frac{\rho g^2(k,l)}{2mN^2} \left(\frac{T_A}{T_0} \right)^2 \quad (15)$$

645 where ρ is air density. This quantity is conserved as a wave propagates to higher altitudes (Ern et
 646 al., 2015), and hence mean $|F|$ over a vertical column adequately describes the amount of wave
 647 activity over the entire column.

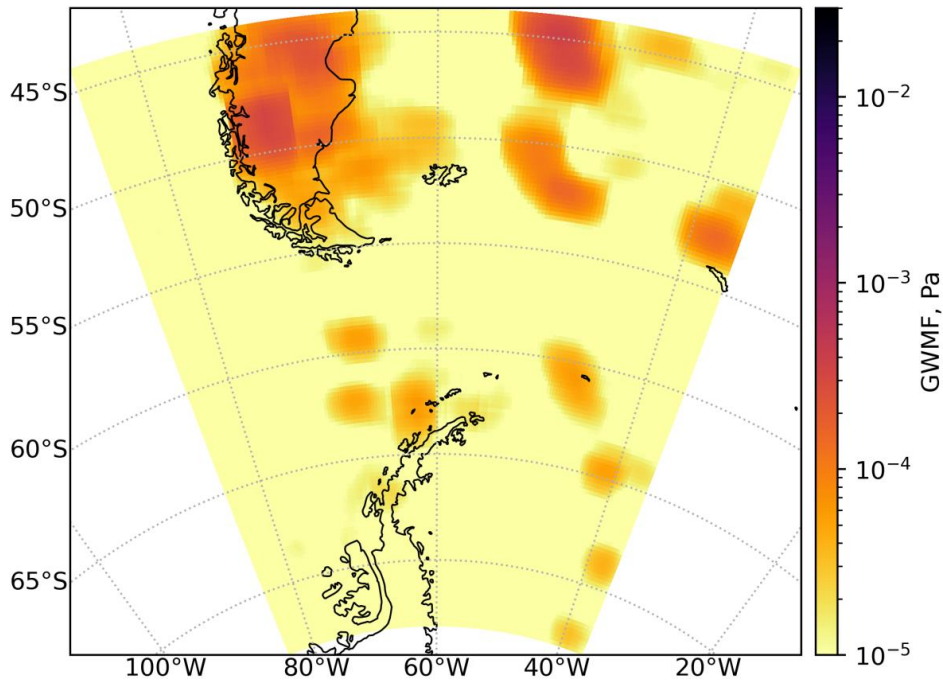
648 The results are presented in Figures 22 and 23. For greater data reliability, heavily overlapping
 649 S3D boxes were used. Each box measures 300 km by 300 km by 6 km, while box centers lie on a
 650 rectangular grid with 0.5 km spacing in the vertical, 0.2° spacing in the meridional direction and
 651 0.3° spacing in the zonal direction. To produce Figures 22 and 23, mean $|F|$ for each vertical
 652 column of boxes was first computed. Then, every grid point in the Figures was assigned a 300
 653 km by 300 km square centered at that point. $|F|$ value for this point was then computed as a mean
 654 of all vertical profiles with footprints overlapping the square, weighted by the area of the
 655 overlap.

656 A comparison of, for example, Figure 11 against Figures 23 and 23 reveals generally similar
 657 results in the most important regions considered here: upward propagating GWs dominate over
 658 the South America and Antarctic Peninsula, while areas with more downward propagation can be
 659 found over the Atlantic.



660

661 **Figure 22.** Mean gravity wave momentum flux of upward propagating waves, in the altitude
662 range from 3 km to 24 km.



663

664 **Figure 23.** Mean gravity wave momentum flux of downward propagating waves, in the altitude
665 range from 3 km to 24 km.

666 It is worth recalling that a few years ago, in a study of GWs over Antarctica, Hertzog et al.
667 (2008) observed, from long-duration superpressure balloon flights at stratospheric levels,
668 mountain waves accounting for about two thirds of the total momentum flux. They found zonally
669 averaged fluxes over the ocean similar in magnitude to those above the continent, underlining the
670 importance of non-orographic GWs in the Southern Hemisphere polar and subpolar latitudes.

671 **6 Conclusions**

672 Based on IFS simulations, a rotary spectral, semi-quantitative classification of GWs is proposed
673 according to their sources: orographic or non-orographic. Their degree of polarization is the main
674 factor taken into account, from non-hydrostatic, non-rotating hydrostatic to rotating GWs,
675 following their intrinsic frequency regimes. An alternative analysis may be to look at the time
676 dependence (standing or non-stationary waves). This option can be performed on the basis of
677 mesoscale simulations and is left for a future contribution.

678 In the extremely complex scenario of upward and downward GW packets found during one of
679 the SOUTHTRAC flights (Flight 08) above the southern Andes, Patagonia, the Antarctic
680 Peninsula and the surrounding oceanic areas, the rotary-vector analysis method was applied. It is
681 based on the Fourier transformation of a complex vector consisting in the perturbations to zonal
682 and meridional wind components with vertical wavelengths less or equal than 15 km. It should
683 be stressed that low frequency GWs are not exactly circularly polarized, except near the inertia
684 frequency, and that even a purely upward or downward wave contributes to both the clockwise
685 and counter-clockwise spectrum. In this sense, this analysis should be considered useful in a
686 statistical sense. Moreover, based on its polarization nature alone, an identification of its likely
687 sources can be made.

688 After a comparison between IFS simulations and lidar data obtained during one of the flights
689 performed during the Southtrac Experiment, the region under study was divided into 2 disjoint
690 vertical intervals. Here, the expected relevance of the polar night jet core in the radiation of GWs
691 was taken into account.

692 In the lower height interval, the main energy flux is concentrated in the lower harmonics. A net
693 larger downgoing energy flux is observed above the overall geographic sector, taking into
694 account that most of it is covered by oceanic areas. Downward GW energy flux suggests the

695 possible relative relevance of inertia GWs, generated after geostrophic imbalance close to or at
696 polar night jet levels and/or in the presence of a front. Instead, if we compute upward GW energy
697 flux per unit area, this is larger than the downward one, because it is concentrated in limited sub-
698 regions, mostly corresponding to mountain areas. In general, upgoing GW energy flux sub-
699 regions are mostly situated above Patagonia, Antarctic Peninsula and several oceanic sectors
700 where other sources like convection or frontal regions may be relevant enough. The latter
701 alternate with sub-regions dominated by LP GWs. Downstream GW sectors only appear above
702 the sea. As mentioned above, they represent the main contribution in terms of relative areas, but
703 not in terms of relative energy flux contribution of the overall region. The relative coverage of
704 upgoing zones with different degrees of polarization strongly depends on the two thresholds
705 proposed in this paper.

706 In particular, by illustrating the GW activity for harmonic #3, which corresponds to a vertical
707 wavelength of 8.3 km, two sub-regions with upwards propagating GW energy above continental
708 areas in central Patagonia and the Antarctic Peninsula show different degrees of elliptic
709 polarization. Above southern Patagonia and Tierra del Fuego Island, there is a predominance of
710 LP GWs, suggesting their orographic origin. Above the remaining oceanic areas, there is a broad
711 distribution of intense up- and downward energy flux, in particular, at and near to the jet and the
712 jet streak position. As mentioned before, possible sources for this variability may be found in
713 departures from geostrophic equilibrium near to the jet. We summarize the dominant GWs in
714 each sub-region by plotting their latitude-longitude distribution in four areas labeled "0" to "3".
715 The labels "0", "1", "2" and "3" indicate, respectively, CR values with negligible total rotational
716 energy, downward, LP and upward dominant GW energy flux. The relative coverage of each of
717 them depends on the thresholds arbitrarily chosen to define the low-energy and linearly polarized
718 GWs.

719 In the upper height interval, the total available GW energy per unit mass is, on average, five
720 times larger than at lower levels. Also, both the total upward GW energy flux and the upward
721 GW energy flux per unit area are weaker here than the respective downward magnitudes. This is
722 contrary to what is observed in the lower height interval. The cumulative effect on C_R and E_T
723 through the vertical wavenumber indicates upward and downward flows with significant
724 deviations from linear polarization. These are observed east of the 75W meridian and in the

725 South Pacific. This is also observed in E_T . Regions with different degrees of polarization, where
726 downward flows dominate, are systematically distributed in elongated bands. These are of
727 different widths and have a predominantly NW-SE direction. These strips are also clear when
728 labeled in four groups as described above.

729 The information to be extracted from the 3 coefficients, C_R , E_T and NC_R is in some sense,
730 complementary. The features and conclusions drawn from each image shown in each one of the
731 6 attached videos are valid only for the corresponding harmonic and completely different from
732 the remaining harmonics.

733 Finally, using the same IFS simulations, we analyze the phase difference between temperature
734 and vertical wind. In doing so, we determine the vertical propagation direction of GWs in the
735 lower height range based on the phase difference between the temperature and vertical wind
736 disturbances. The relative increase of upward GWs with respect to downward GWs above and
737 near the southern Andes and the Antarctic Peninsula, as well as their geographical distribution, is
738 in agreement with our results in section 4.1.

739 A spectral rotary analysis from mesoscale numerical simulations exhibiting a four-dimensional
740 context for the GWs is left for a future contribution. Recently, a study complementary to the one
741 presented here and based on mesoscale simulations during flight 08 is provided by Alexander et
742 al. (submitted). Version 4.2 of the ARW Weather Research and Forecasting (WRF) model is
743 forced with initial and boundary conditions from the 0.25 x 0.25 degree ERA5 reanalyses
744 provided hourly. Data are available at 137 levels from 1000 to 0.01 hPa. The solution has 150
745 vertical levels and the authors compare the model results with measurements obtained during
746 SOUTHTRAC-GW. In particular, the possible coexistence and interaction of orographic and
747 non-orographic gravity waves is evaluated.

748 **Acknowledgments**

749 AT, PA, RH, PL and TM were funded by grants ANPCYT PICT 2018-653 and PIP-
750 CONICET20170100067

751

752 **Open Research**

753 **References**

754 Alexander, M. J. (1998). Interpretations of observed climatological patterns in stratospheric
755 gravity wave variance, *J. Geophys. Res.*, 103, 8627–8640. <https://doi.org/10.1029/97JD03325>

756 Alexander, M. J., M. Geller, C. McLandress, S. Polavarapu, P. Preusse, Sassi, F., et al. (2010).
757 Recent developments in gravity wave effects in climate models, and the global distribution of
758 gravity wave momentum flux from observations and models, *Q. J. Roy. Meteorol. Soc.*, 136,
759 1103-1124, <https://doi.org/10.1002/qj.637>

760 Alexander, P., & de la Torre, A. (2010). A Method to Infer the Three Cartesian Wavelengths of a
761 Mountain Wave from Three Soundings, *J. Appl. Meteor. Climatol.*, 49, 2069–2074.
762 <https://doi.org/10.1175/2010JAMC2348.1>

763 Alexander, P., de la Torre, A., Hierro, R., & Llamedo, P. (2015a). Assessment of precision in
764 ionospheric electron density profiles retrieved by GPS radio occultations, *Adv. Space Res.*,
765 <http://dx.doi.org/10.1016/j.asr.2014.08.029>, 54, 2249-258

766 Alexander, P., de la Torre, A., Schmidt, T., Llamedo, P., & Hierro, R. (2015b). Limb sounders
767 tracking topographic gravity wave activity from the stratosphere to the ionosphere around
768 midlatitude Andes, *J. Geophys. Res.*, 120. <https://doi.org/10.1002/2015JA021409>

769 Alexander, P., Schmidt T., & de la Torre, A. (2018). A method to determine gravity wave net
770 momentum flux, propagation direction, and “real” wavelengths: A GPS radio occultations
771 soundings case study. *Earth and Space Science*, 5. <https://doi.org/10.1002/2017EA000342>

772 Alexander, P., et al. (2022). The coexistence of gravity waves from diverse sources during a
773 SOUTHTRAC flight with optimal vertical propagation conditions. *J. Geophys. Res.*(to be
774 submitted to this issue)

775 Bramberger, M., Dörnbrack A., Bossert K., Ehard B. , Fritts D.C., Kaifleret B., et al. (2017).
776 Does strong tropospheric forcing cause large-amplitude mesospheric gravity waves? A
777 DEEPWAVE case study. *J. Geophys. Res. Atmos.*, 122, 11 422–11 443.
778 <https://doi.org/10.1002/2017JD027371>

- 779 Bramberger, M., Dörnbrack, A., Wilms, H., Ewald, F., & Sharman, R. (2020). Mountain-wave
780 turbulence encounter of the research aircraft HALO above Iceland. *J. Appl. Meteor.*
781 *Climatol.*, 59, 567–588. <https://doi.org/10.1175/JAMC-D-19-0079.1>
- 782 Cadet, D., & Teitelbaum, H. (1979). Observational evidence of internal inertia-gravity waves in
783 the tropical stratosphere. *J. Atmos. Sci.*, 36, 892-907
- 784 Cho, J.Y.N. (1995). Inertio-gravity wave parameter estimation from crossspectral analysis. *J*
785 *Geophys Res*, 100:18727–18737. <https://doi.org/10.1029/95JD01752>
- 786 Gill, A.E. (1982). *Atmosphere and Ocean Dynamics*, Academic Press, New York
- 787 Gubenko, V.N., Kirillovich1, I. A., & Andreev, V.E. (2020). Improvement of methods for
788 studying internal gravity waves in the Earth's atmosphere using radiosonde measurements, *J.*
789 *Phys.: Conf. Ser.* 1632 012007
- 790 Hertzog, A., Boccara, G., Vincent, R., Vial, F., & Cocquerez, P. (2008). Estimation of gravity
791 wave momentum flux and phase speeds from quasi-lagrangian stratospheric balloon Flights. Part
792 II: Results from the Vorcore Campaign in Antarctica, *J. Atmos. Sci.*, 65, 10, 3056-3070,
793 <https://doi.org/10.1175/2008JAS2710.1>
- 794 Hindley, N.P., Wright, C.J., Smith, N.D., & Mitchell, N.J. (2015). The southern stratospheric
795 gravity wave hotspot: individual waves and their momentum fluxes measured by COSMIC GPS-
796 RO, *Atmos. Chem. Phys.*, 15, 7797–7818. <https://doi.org/10.5194/acp-15-7797-2015>
- 797 Hines, C.O. (1991). The saturation of gravity waves in the middle atmosphere. Part I: Critique of
798 linear instability theory, *J. Atmos. Sci.*, 48, 1348-1359
- 799 Hirota, I., & Niki, T. (1985). A Statistical Study of Inertia-Gravity Waves in the Middle
800 Atmosphere, *J. M. Soc. Jap*, 63, 6, 1055-1066
- 801 Hoffmann, L., Grimsdell, A. W., & Alexander, M. J. (2016). Stratospheric gravity waves at
802 Southern Hemisphere orographic hotspots: 2003 –2014 AIRS/Aqua observations, *Atmos. Chem.*
803 *Phys.*, 16, 9381–9397. <https://doi.org/10.5194/acp-16-9381-2016>

- 804 Kaifler, N., Kaifler, B., Dörnbrack, A., Rapp, M., Hormaechea, J. L., & de la Torre, A. (2020).
805 Lidar observations of large-amplitude mountain waves in the stratosphere above Tierra del
806 Fuego, Argentina, *Sci. Rep.*, *10*, 14529. <https://doi.org/10.1038/s41598-020-71443-7>
- 807 Krisch, I., Preusse P., Ungermann, J., Dörnbrack, A., Eckermann, S.D., & Ern, M. (2017). First
808 tomographic observations of gravity waves by the infrared limb imager GLORIA. *Atmos. Chem.*
809 *Phys.*, **17**, 14 937–14 953. <https://doi.org/10.5194/acp-17-14937-2017>
- 810 Leaman, K. D., & Sanford, T. B. (1975). Vertical energy propagation of inertial waves: A vector
811 spectral analysis of velocity profiles, *J. Geophys. Res.*, *80*, 1975-1978.
812 <https://doi.org/10.1029/JC080i015p01975>
- 813 Lehmann, C. I., Kim, Y.H., Preusse, P., Chun, H.Y., Ern, M., & Kim, S.Y. (2012).
814 Consistency between Fourier transform and small-volume few-wave decomposition for spectral
815 and spatial variability of gravity waves above a typhoon. *Atmos. Meas. Tech.*, *5*(7), 1637-1651.
816 <https://doi.org/10.5194/amt-5-1637-2012>
- 817 Llamedo, P., Salvador, J., de la Torre, A., Quiroga, J., Alexander, P., Hierro, R., et al. (2019). 11
818 years of Rayleigh lidar observations of gravity wave activity above the southern tip of South
819 America, *J. Geophys. Res. Atmos.*, *124*, 451–467. <https://doi.org/10.1029/2018JD028673>
- 820 Mishchenko, M. I. (2014). *Electromagnetic Scattering by Particles and Particle Groups: An*
821 *Introduction*, Cambridge University Press, Cambridge
- 822 Mooers, C. N. K. (1973). A technique for the cross spectrum analysis of pairs of complex-valued
823 time series, with emphasis on the properties of polarized components and rotational invariants,
824 *Deep Sea Reli.*, *20*, 1129-1141
- 825 Plougonven, R., & F. Zhang (2014). Internal gravity waves from atmospheric jets and fronts,
826 *Rev. Geophys.*, *52*. <https://doi.org/10.1002/2012RG000419>
- 827 Polichtchouk, I., et al. (2021). Stratospheric Modelling and Assimilation, ECMWF Technical
828 Memorandum

- 829 Portele, T. C., Dörnbrack, A., Wagner, J. S., Gisinger, S., Ehard, B., Pautet, P.D., et al. (2018).
830 Mountain-wave propagation under transient tropospheric forcing: A DEEPWAVE case study.
831 *Mon. Wea. Rev.*, **146**, 1861–1888. <https://doi.org/10.1175/MWR-D-17-0080.1>
- 832 Rapp, M., Kaifler, B., Dörnbrack, A., Gisinger, S., Mixa, T., Reichert, R., et al. (2021).
833 SOUTHTRAC-GW: An Airborne Field Campaign to Explore Gravity Wave Dynamics at the
834 World's Strongest Hotspot. *Bull. Amer. Meteor. Soc.*, *102* (4), E871 - E893. <https://doi.org/10.1175/BAMS-D-20-0034.1>
- 836 Riese, M., Oelhaf, H., Preusse, P., Blank, J., Ern, M., Friedl-Vallon, F., et al. (2014). Gimballed
837 Limb Observer for Radiance Imaging of the Atmosphere (GLORIA) scientific objectives. *Atmos.*
838 *Meas. Tech.*, **7**, 1915–1928. <https://doi.org/10.5194/amt-7-1915-2014>
- 839 Skamarock, W., & J. B. Klemp (2008). A time-split nonhydrostatic atmospheric model for
840 weather research and forecasting applications, *J. Comput. Phys.*, *227*, 3465–3485. <https://doi.org/10.1016/j.jcp.2007.01.037>
- 842 Smith, R. B., Nugent, A. D., Kruse, C. G., Fritts, D. C., Doyle, J. D., Eckermann, S. D., et al.
843 (2016). Stratospheric Gravity Wave Fluxes and Scales during DEEPWAVE, *Journal of the*
844 *Atmospheric Sciences*, *73*(7), 2851-2869. <https://doi.org/10.1175/JAS-D-15-0324.1>
- 845 Vadas, S. L. (2013). Compressible f -plane solutions to body forces, heatings, and coolings, and
846 application to the primary and secondary gravity waves generated by a deep convective plume, *J.*
847 *Geophys. Res. Space Physics*, *118*, 2377–2397, doi:10.1002/jgra.50163
- 848 Vincent, R.A. (1984). Gravity-wave motions in the mesosphere, *J. Atmos. Terr. Phys.*, *46*, 2, 119-
849 128
- 850 Vincent, R.A., & Fritts, D.C. (1987). A Climatology of Gravity Wave Motions in the Mesopause
851 Region at Adelaide, Australia, *J. Atmos. Sci.*
852 [https://doi.org/10.1175/15200469\(1987\)044<0748:ACOGWM>2.0.CO;2](https://doi.org/10.1175/15200469(1987)044<0748:ACOGWM>2.0.CO;2)
- 853 Vincent, R. A., & Alexander, M. J. (2020). Balloon-borne observations of short vertical
854 wavelength gravity waves and interaction with QBO winds. *J. Geophys. Res.–Atmos.*, *125*,
855 e2020JD032779. <https://doi.org/10.1029/2020JD032779>

- 856 Wickert, J., Arras, C., Brack, A., Dick, G., Kepkar, A., Männel, B., et al. (2021). Ground and
857 Space based GNSS for Space Weather Monitoring at GFZ: Overview and Recent Results -
858 *Abstract Book, IAG 2021*
- 859 Wilms, H., Bramberger, M., & Dörnbrack, A. (2020). Observation and simulation of mountain
860 wave turbulence above Iceland: Turbulence intensification due to wave interference. *Quart. J.*
861 *Roy. Meteor. Soc.*, **146**, 3326–3346. <https://doi.org/10.1002/qj.3848>
- 862 Wu, D. L., Preusse, P., Eckermann, S.D., Jonathan, H. J., de la Torre, M.J., Coy, L., et al. (2006).
863 Remote sounding of atmospheric gravity waves with satellite limb and nadir techniques, *Adv.*
864 *Space Res.*, *37*, 22692277
- 865 Zhang, F., Wang, S., & Plougonven, R. (2004). Potential uncertainties in using the hodograph
866 method to retrieve gravity wave characteristics from individual soundings, *Geophys. Res. Lett.*,
867 *31* (L11110).<https://doi.org/10.1029/2004GL019841>